In: Eulerian Codes for the Numerical Solution ... ISBN 978-1-61668-413-6
Editor: Magdi Shoucri, pp. 87-120

Chapter 4

EULERIAN-LAGRANGIAN KINETIC SIMULATIONS OF LASER-PLASMA INTERACTIONS

***David J. Strozzi*[1]*, *A. B. Langdon*[1], *E. A. Williams*[1], *A. Bers*[2], *and S. Brunner*[3]**
[1] AX Division, Lawrence Livermore National Laboratory, Livermore, CA, 94550, USA
[2] Massachusetts Institute of Technology, Cambridge, MA, 02139, USA
[3] Ecole Polytechnique Fédérale de Lausanne, 1015 Lausanne, Switzerland

Abstract

The Eulerian Vlasov-Maxwell solver ELVIS is described, and applied to electrostatic and laser-plasma interaction problems, in this chapter. The code treats the plasma kinetically in one longitudinal dimension, either non-relativistically or relativistically, and optionally including a Krook relaxation operator. The transverse dynamics comprise linearly polarized light waves and a cold, collisionless fluid. The kinetic equation is solved via operator splitting, with 1D space and momentum advections performed by solution along characteristics with cubic spline interpolation. The Landau damping of a Langmuir wave, created as an initial density perturbation, is studied non-relativistically and relativistically (the damping is reduced in the latter case for high temperatures). Nonlinear trapping of electrons in the wave's potential well, and the resulting decrease of Landau damping, is also demonstrated. Simulations with ELVIS of backward stimulated Raman scattering (SRS) of a high-intensity laser, for parameters appropriate to inertial confinement fusion, are presented. Kinetic inflation, or enhancement, of the SRS reflectivity (due to trapping-induced damping reduction) above that of coupled-mode, linear-damping calculations is shown in conditions relevant to single laser speckle experiments at the Trident laser facility. In addition, the generation of electron acoustic waves (and Thomson-like laser scattering off them) by the beating of SRS-produced beam-acoustic modes is shown. The inclusion of a Krook operator, to mimic transverse electron loss out of a finite speckle, imposes a threshold for inflation, which gradually develops as resonant electrons complete $\gtrsim$ one bounce orbit before being detrapped. The use of a broadband scattered-light seed very slightly decreases the reflectivity below that given by a monochromatic seed.

*E-mail address: strozzi2@llnl.gov

Keywords: Eulerian kinetic simulation, method of characteristics, Vlasov-Maxwell solver, Landau damping, Krook operator, Langmuir waves, laser-plasma interactions, stimulated Raman scattering, electron acoustic waves.

1. Introduction

Kinetic equations, which describe the evolution in phase space of particle distribution functions, comprise some of the most fundamental descriptions of plasma dynamics. The rich physics and extreme detail contained in such models is accompanied by the severe challenges involved in their theoretical and numerical solution. While fluid or other reduced models can frequently be employed, there are important cases where a kinetic description is necessary (and discussed in this book).

This present chapter is concerned with kinetic simulations related to laser-plasma interactions [1]. In particular, we will focus on physics relevant to stimulated Raman scattering (SRS), a resonant, three-wave parametric process where a pump electromagnetic wave (EMW), such as a laser, decays into a scattered EMW and a Langmuir wave (LW). SRS is the basis of several applications, including laser-based particle acceleration [2] and the backward Raman amplifier [3]. Moreover, for laser-driven inertial confinement fusion (ICF) [4, 5] experiments like the National Ignition Facility (NIF) [6] and Laser Mégajoule (LMJ) [7] to succeed, SRS and other laser-plasma instabilities must not be too active. Since SRS removes energy from the pump laser, it can prevent the desired energy from being delivered to the target, with the desired spatial and temporal behavior. NIF experiments on hohlraum energetics in late 2009 showed significant (but acceptable) SRS from the "inner" cone of beams [8].

The Langmuir wave in SRS resonates with electrons moving at the wave phase velocity, which gives rise to linear Landau damping [9]. For a finite-amplitude wave, electrons can be "trapped" in the wave's (nearly) sinusoidal potential. This causes several nonlinear effects, including the reduction in Landau damping [10], the downshift in LW frequency [11, 12], the trapped-particle modulation instability [14], and Langmuir-wave self-focusing or filamentation [15, 16]. The distortion of the electron distribution near the wave phase velocity produces a population of energetic or "hot" electrons. From the standpoint of achieving ICF, these electrons can irreversibly pre-heat the fuel capsule and thereby reduce the fuel compression (which degrades rapidly as entropy is added).

These processes are all fundamentally kinetic, which is a major motivation for kinetic SRS simulations. Analytic progress has also been made in understanding and modeling these effects. We will not attempt here to review recent theoretical and numerical work in kinetic modeling of SRS, but will briefly mention a few highlights.

In this chapter, we will discuss kinetic simulations relevant to SRS, performed with a 1D Eulerian Vlasov-Maxwell solver called ELVIS. These include electrostatic studies with no laser included, such as the linear and nonlinear damping of Langmuir waves. We shall show that the damping rate in a high-temperature (17 keV) plasma is greatly reduced when a relativistic instead of non-relativistic model is used. Electromagnetic simulations with a pump laser will explore the enhancement or "inflation" of SRS due to Landau damping reduction [17, 18], along with scattering off electron acoustic waves indirectly generated by SRS. We explore the threshold for trapping to overcome relaxation (represented by a Krook

operator, intended to model multi-D particle side loss out of a laser speckle), along with the role of bandwidth in the seed scattered light wave.

The chapter is organized as follows. Section 2 describes the model and numerical method of the ELVIS code. The code is applied to electrostatic problems concerning the non-relativistic and relativistic evolution of an LW in section 3. SRS simulations with and without Krook relaxation are presented in section 4, which is followed by the conclusion.

2. ELVIS Equations and Numerical Method

ELVIS (which stands for Eulerian-Lagrangian Vlasov Integrator with Splines) is a serial Vlasov-Maxwell solver, with kinetic longitudinal dynamics, cold-fluid transverse dynamics, and linearly-polarized transverse electromagnetic (e/m) fields. Time evolution is "leapfrogged" in that the particle distribution function f is known at whole timesteps, while the transverse e/m fields are known at half steps. Operator splitting is used in time for the kinetic equation, such that the phase-space advections (in space and momentum) of f are done separately. These 1D advections are performed via the method of characteristics (also called the semi-Lagrangian or Eulerian-Lagrangian method). Cubic splines are used to interpolate f at the "foot" of characteristics, which are simply the particle orbits. The code is similar to the parallel code SAPRISTI [14, 19], and also to the non-periodic code described in [20] (Ref. [21] details its periodic version).

ELVIS is a rather modest code by current standards, and is far from the cutting edge of massively parallel, multi-D Vlasov codes using high-order methods. We are still able to productively use it for physics problems. ELVIS is documented and applied extensively to electrostatic problems and SRS in Ref. [22], as well as Refs. [23, 24, 18, 25, 26].

2.1. Model and geometry

ELVIS employs a simple 1D model which allows for SRS to be studied kinetically. Spatial variations (gradients and wave vectors) are all in the x (longitudinal) direction. The particle dynamics in x are described by a kinetic equation, consisting of a collisionless Vlasov operator which includes the x component of the $\vec{v} \times \vec{B}$ (ponderomotive) force from the transverse electromagnetic fields. In addition, a Bhatnagar-Gross-Krook, often called simply a Krook, operator is included [27], both to mimic dissipation (such as transverse sideloss out of a localized laser speckle) and for numerical damping near boundaries. The transverse dynamics describe light waves linearly polarized in y, and the particles are described as a cold, collisionless, non-relativistic fluid with a y velocity. Fig. 1 presents the geometry, with profiles relevant to SRS in a finite system.

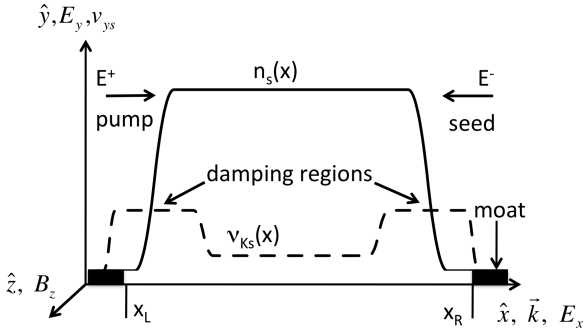

Figure 1. Geometry of the ELVIS code, illustrated for a laser backscatter problem in a finite density profile.

The governing equations in normalized "ELVIS" units are:

$$\left[\partial_t + v_x\partial_x + Z_s\left(E_x + v_{ys}B_z\right)\partial_{p_x}\right] f_s = \nu_{Ks}(x)\left(n_s\hat{f}_{0s} - f_s\right), \quad (1)$$

$$\partial_x E_x = \rho \equiv \sum_s Z_s n_s, \quad (2)$$

$$\mu_s\partial_t v_{ys} = Z_s E_y, \quad (3)$$

$$\left(\partial_t \pm \partial_x\right) E^{\pm} = -J_y \equiv -\sum_s Z_s n_s v_{ys}, \quad (4)$$

$$E^{\pm} \equiv E_y \pm B_z. \quad (5)$$

Note that $E_y = (1/2)(E^+ + E^-)$ and $B_z = (1/2)(E^+ - E^-)$. ELVIS units are such that length, time, mass, charge, and number density are scaled to $d_{e0} = c/\omega_{p0}$, $1/\omega_{p0}$, m_e, e, and n_0, where m_e is the electron mass, $e > 0$ the positron charge, n_0 is a reference number density, and $\omega_{p0}^2 = n_0 e^2/\varepsilon_0 m_e$ is the electron plasma frequency for n_0. $\mu_s = m_s/m_e$ and $Z_s e$ are the relative mass and charge of species s; $s = e$ for electrons, $Z_e = -1$. We use ELVIS or physical SI units as convenient (which should be clear by context), and write $X_{\rm elv}$ or $X_{\rm phys}$ to explicitly indicate units. We drop the s subscript when this leads to no ambiguity.

The 1D particle distribution $f_s(x, p_x, t)$ is normalized such that $n_s \equiv \int dp_x\ f_s$ is the volumetric number density. The x velocity v_x is related to momentum p_x by $v_x = u_x/\gamma_x$, where $\vec{u} = \vec{p}_{\rm phys}/m_s c = \vec{p}_{\rm elv}/\mu_s$ is always unitless. $\gamma_x = 1$ or $[1 + u_x^2]^{1/2}$ for non-relativistic or relativistic modes, respectively. The relativistic mode excludes transverse motion from the Lorentz factor γ_x, and is thus only appropriate for $v_{ys} \ll c$. It is valid for studying strictly 1D relativistic dynamics. A number-conserving Krook relaxation operator is included, with relaxation rate $\nu_{Ks}(x)$ and a normalized equilibrium distribution $\hat{f}_{0s}$ (usually set to a thermal Maxwellian), $\int dp_x\ \hat{f}_{0s} = 1$.

To understand the transverse dynamics, we write the "full" distribution function as $F(x, p_x, P_y, p_z) = f(x, p_x)\delta(P_y)\delta(p_z)$ where δ denotes the Dirac delta function, P_y is the canonical y momentum, and we ignore z motion. Our y momentum equation is just the conservation law $P_y = 0$, sometimes called Gabor's theorem [28]. This is justified as follows. Consider a warm, non-relativistic fluid momentum equation with isotropic pressure, in physical units:

$$m(\partial_t + \vec{v}\cdot\nabla)\vec{v} = q(\vec{E} + \vec{v}\times\vec{B}) - n^{-1}\nabla p. \quad (6)$$

Introducing potentials via $\vec{E} = -\nabla\phi - \partial_t\vec{A}$, $\vec{B} = \nabla\times\vec{A}$, and an equation of state such that $n^{-1}\nabla p = \nabla g(n)$, this becomes

$$\partial_t\vec{P} = \vec{v}\times\nabla\times\vec{P} - \nabla G \tag{7}$$

with $\vec{P} \equiv m\vec{v} + q\vec{A}$ the canonical momentum and $G \equiv \frac{1}{2}mv^2 + q\phi + g$. Taking the curl of this, we find

$$\partial_t\vec{C} = \nabla\times(\vec{v}\times\vec{C}), \qquad \vec{C} \equiv \nabla\times\vec{P}. \tag{8}$$

Clearly, if $\vec{C} = 0$ initially, it remains so for all time. This obtains, for instance, if a plasma initially free of transverse fields or motion is irradiated by a laser introduced from vacuum. For our geometry, $\nabla \to \partial_x$, and $C_z = \partial_x P_y$ remains zero for all time. If P_y at some x (say, far from the laser) is zero for all time, then $P_y(x,t) = 0$.

We use the combinations $E_\pm$ of the transverse e/m fields E_y and B_z since they each satisfy a 1D advection equation which requires a single incoming boundary condition, suffers no numerical reflection at the outgoing boundary, and is readily solvable by shifts of one gridpoint if $\Delta x = c\Delta t$ (see Sec. 2.6.).

2.2. Structure of the timestep

We employ a "leapfrog" scheme where f, and instantaneous functions of it like n and E_x, are stored at whole timesteps $t_n = n\Delta t$, and the transverse e/m fields $E^\pm$ are stored at half steps $t_{n-1/2}$. Only uniform grids are currently employed by ELVIS, and treated here. v_y is needed at both whole and half steps, since it appears in both the f and $E^\pm$ time advance. All spatial functions are known at whole gridpoints $x_j = j\Delta x$. For electrostatic problems (no transverse fields $E^\pm$ or v_{ys}), Δt and Δx are unrelated, and there is no Courant stability condition due to the way we advance f along characteristics. However, for problems with transverse fields we require $\Delta x = \Delta t$ since we advance $E^\pm$ by shifting them by exactly one gridpoint every timestep (see Sec. 2.6.).

The complete time advance, from time t_0 to t_1, is given in Fig. 2, and is described as follows:

1. $S_{1/2}$ (stream): advance f_s for $\Delta t/2$, from $f_{s,0}$ to $f^{--}_{s,1/2}$, via $(\partial_t + v_x\partial_x)f_s = 0$.

2. Using $f^{--}_{s,1/2}$, compute $n_{s,1/2}$, $\rho_{1/2} = \sum_s Z_s n_{s,1/2}$, and $E_{x,1/2}$ from Gauss' law. These quantities have valid values at $t_{1/2}$ since the A and K operators both leave n_s unchanged.

3. $K_{1/2}$ (Krook): advance f_s for $\Delta t/2$, from $f^{--}_{s,1/2}$ to $f^{-}_{s,1/2}$, via $\partial_t f_s = \nu_{Ks}(n_{s,1/2}\hat{f}_{0s} - f_s)$.

4. M_1 (Maxwell): Advance $E^\pm$ by Δt from $E^\pm_{-1/2}$ to $E^\pm_{1/2}$ via $(\partial_t \pm \partial_x)E^\pm = -J_{y,0}$ where $J_{y,0} = \sum_s Z_s n_{s,0} v_{ys,0}$.

5. Y_1 (y accelerate): Advance v_{ys} for Δt via $v_{ys,1} = v_{ys,0} + (Z_s/2\mu_s)(E^+_{1/2} + E^-_{1/2})$.

6. Find $v_{ys,1/2} = (1/2)(v_{ys,0} + v_{ys,1})$. This auxiliary variable is needed in the x force in the Vlasov acceleration, but is directly dependent only on v_{ys} at whole timesteps.

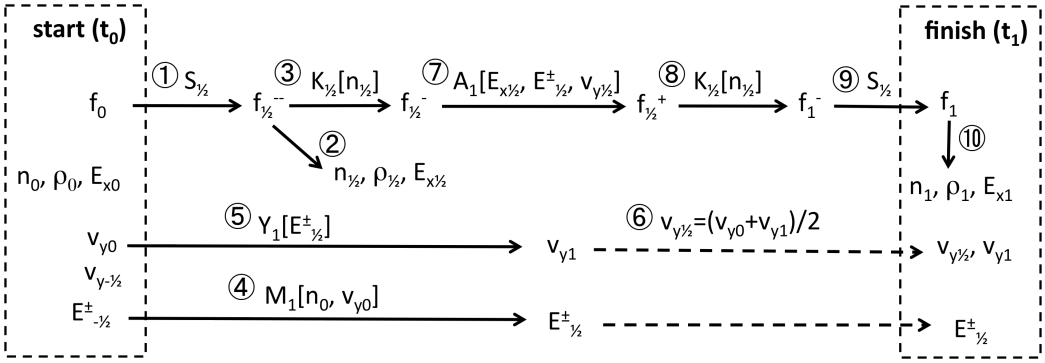

Figure 2. Diagram of one ELVIS timestep from time t_0 to t_1.

7. A_1 (accelerate): advance f_s for Δt, from $f^-_{s,1/2}$ to $f^+_{s,1/2}$, via $(\partial_t + F_{xs,1/2}\partial_{p_x})f_s = 0$ where $F_{xs,1/2} = Z_s[E_{x,1/2} + (1/2)v_{ys,1/2}(E^+_{1/2} - E^-_{1/2})]$ is the x force at $t_{1/2}$.
8. $K_{1/2}$: advance f_s for $\Delta t/2$, from $f^+_{s,1/2}$ to $f^-_{s,1}$, via Krook operator as in step 3.
9. $S_{1/2}$: advance f_s for $\Delta t/2$, from $f^-_{s,1}$ to $f_{s,1}$, via free streaming as in step 1.
10. Using $f_{s,1}$, compute $n_{s,1}$, ρ_1, and $E_{x,1}$ as in step 2.

The kinetic equation for f is solved via operator splitting [29, 30], first applied to Vlasov codes by Cheng and Knorr [31]. Consider a generic time-evolution equation

$$\frac{df}{dt} = Hf, \qquad H = H_1 + H_2, \tag{9}$$

where H_i is an operator on the variables f. The exact solution for a timestep Δt is $U(\Delta t)f_0$ where $U(t) = \exp Ht$ and f_0 is an initial condition (IC). The splitting theorem states that given two approximate operators U^a_i which are second-order accurate, i.e. $(U^a_i(\Delta t) - U_i(\Delta t))f_0 = O(\Delta t^3)$, we can construct an operator U^a which is a second-order accurate approximation to U via

$$U^a(\Delta t) = U^a_1(\Delta t/2)U^a_2(\Delta t)U^a_1(\Delta t/2). \tag{10}$$

This can be verified by computing $U^a(\Delta t) - \exp H\Delta t$ for non-commuting H_i (which is generally the case for the operators we consider), and is related to the Baker-Campbell-Hausdorff formula for Lie groups.

The method is directly extended to multiple operators, e.g. for three operators we have

$$U^a(\Delta t) = U^a_1(\Delta t/2)U^a_2(\Delta t/2)U^a_3(\Delta t)U^a_2(\Delta t/2)U^a_1(\Delta t/2). \tag{11}$$

This is precisely the case for our kinetic equation, which involves operators $S = U^a_1$, $K = U^a_2$, and $A = U^a_3$ for free streaming, the Krook operator, and acceleration respectively. In the timestep notation used above, the kinetic equation is split as follows:

$$U^a(\Delta t) = S_{1/2}K_{1/2}A_1K_{1/2}S_{1/2}. \tag{12}$$

2.3. f advection: cubic splines

The space and momentum advections in the kinetic equation are both performed as separate 1D shifts along characteristics (called a semi-Lagrangian or Eulerian-Lagrangian method). For concreteness consider the x advection (performed once for each v) $\partial_t f + v\partial_x f = 0$, with solution $f(x,t+\Delta t) = f(x-v\Delta t,t)$. Let $f_j^n = f(x_j,t_n)$, $x_j = j\Delta x$, and $t_n = n\Delta t$. We must find $f_j^{n+1} = f(x_j - v\Delta t, t_n)$ given f_j^n at time t_n. Since $x_j - v\Delta t$ is in general not a gridpoint, we interpolate to find its value. Characteristic methods are usually implicit, in that a set of equations must be solved to carry out the interpolation, and also have no Courant stability condition (see the von Neumann analysis below), since a shift by more than one gridpoint merely requires the interpolation to be done about an x location farther from x_j (of course, accuracy suffers with shifts over many gridpoints). That is, we always interpolate for f_j^{n+1} between known values of f_j^n, and never extrapolate as happens in methods like first-order upwinding when $v\Delta t > \Delta x$ (this is why such methods have a Courant condition).

ELVIS uses cubic spline interpolation, as detailed in App. A.4.3 of [22]. Cubic spline and cubic B-spline interpolation (for uniform and non-uniform grids) is discussed and applied to Vlasov and fluid equations in Ref. [32]. Ref. [33] contains a general discussion of spline and other interpolation applied to advection problems, including details on their numerical dispersion and dissipation. The advantages of cubic splines are low numerical dispersion and dissipation, and the low computational cost of the resulting tridiagonal system of equations. Its drawbacks include that the interpolant can overshoot, or exceed extreme values of the given f_j points (for instance, the interpolant of an initially positive set of f_j can be negative). Moreover, semi-Lagrangian advection does not satisfy a *local* discrete conservation law, as do finite-volume, flux-conservative methods. This problem is not specific to spline interpolants.

ELVIS currently uses only uniform x and p_x grids, which give high-order accuracy but are wasteful in that the finest resolution needed on each grid must be used everywhere. In our particular applications the momentum resolution needs to be highest around the plasma-wave phase velocity where electron trapping occurs, and substantial savings could be had by using a coarser mesh elsewhere. Some results below, namely the tridiagonal system Eq. (21), are only valid for uniform grids.

Cubic spline interpolation entails expressing $f(x)$ as a cubic polynomial $F_j(x)$ about each gridpoint:

$$F_j(X) = f_j + p_j X + s_j X^2 + g_j X^3 \tag{13}$$

where $X = (x - x_j)/\Delta x$. $F_j(0) = f_j$ by construction, and we require continuity at $x = x_j$ of F_j and its first two derivatives with the neighboring interpolant F_{j-1}. These matching conditions give the following system:

$$f_{j-1} + p_{j-1} + s_{j-1} + g_{j-1} = f_j, \tag{14}$$

$$p_{j-1} + 2s_{j-1} + 3g_{j-1} = p_j, \tag{15}$$

$$s_{j-1} + 3g_{j-1} = s_j. \tag{16}$$

Taking linear combinations of these equations at nearby gridpoints gives a tridiagonal sys-

tem for the unknowns in terms of the known f_j's:

$$p_{j+1} + 4p_j + p_{j-1} = -3f_{j-1} + 3f_{j+1}, \tag{17}$$
$$s_{j+1} + 4s_j + s_{j-1} = 3f_{j-1} - 6f_j + 3f_{j+1}, \tag{18}$$
$$g_{j+1} + 4g_j + g_{j-1} = -f_{j-1} + 3f_j - 3f_{j+1} + f_{j+2}. \tag{19}$$

Consider now interpolation for x advection with $v < 0$ for definiteness, involving a shift $\delta = |v|\Delta t$. We assume $\Delta \equiv \delta/\Delta x < 1$ for convenience (as discussed above, shifts by more than Δx pose no difficulty). We approximate the new value of f_j at time $t + \Delta t$, $f_j^{n+1} = \bar{f}_j \equiv f(x_j + \delta)$, by

$$\bar{f}_j \approx F_j(x_j + \delta) = f_j + p_j\Delta + s_j\Delta^2 + g_j\Delta^3. \tag{20}$$

We can form a tridiagonal system for the $\bar{f}_j$, all shifted by the same Δ from x_j (valid only for a uniform grid), in terms of the known f_j, by taking $\bar{f}_{j-1} + 4\bar{f}_j + \bar{f}_{j+1}$:

$$\bar{f}_{j-1} + 4\bar{f}_j + \bar{f}_{j+1} = a_{-2}f_{j+2} + a_{-1}f_{j+1} + a_0 f_j + a_1 f_{j-1}, \tag{21}$$

where

$$a_1 = 1 - 3\Delta + 3\Delta^2 - \Delta^3, \tag{22}$$
$$a_0 = 4 - 6\Delta^2 + 3\Delta^3, \tag{23}$$
$$a_{-1} = 1 + 3\Delta + 3\Delta^2 - 3\Delta^3, \tag{24}$$
$$a_{-2} = \Delta^3. \tag{25}$$

For $v > 0$ the logic is similar, and a unified system for both signs of v is

$$\bar{f}_{j-1} + 4\bar{f}_j + \bar{f}_{j+1} = a_{-2}f_{j-2\sigma} + a_{-1}f_{j-\sigma} + a_0 f_j + a_1 f_{j+\sigma}. \tag{26}$$

with $\sigma \equiv \operatorname{sign} v = \pm 1$. The a's are defined *exactly as for* $v < 0$, with $\delta = |v|\Delta t$ in both cases.

The numerical dispersion and dissipation of advection by interpolation can be studied by a von Neumann analysis. We consider the time evolution of one spatial harmonic of wavelength $2\pi/k$ by writing $f_j^n = g^n \exp[ikx_j]$. Substituting into Eq. (26), we find

$$g \cdot [4 + 2\cos\alpha] = a_{-2}e^{-2i\sigma\alpha} + a_{-1}e^{-i\sigma\alpha} + a_0 f_j + a_1 e^{i\sigma\alpha}, \tag{27}$$

where $\alpha \equiv k\Delta x$. The corresponding solution of the advection PDE $(\partial_t + v\partial_x)f = 0$ is $f = \exp ik(x - vt)$, which gives an analytic amplification factor $g_{\text{an}} = \exp[-ikvt]$. Numerical dissipation or instability is indicated by $|g| \neq 1$ (note $|g_{\text{an}}| = 1$), and the phase error ϕ in one timestep is given by $\phi = \arg[g/g_{\text{an}}]$. Figure 3 presents the dissipation for $\alpha \in [0, \pi]$, or half the Nyquist range $|k| \leq \pi/\Delta x$. The following symmetry relations apply: $|g(-\alpha)| = |g(\alpha)|$, $|g(\sigma = -1)| = |g(\sigma = 1)|$, and $|g(\Delta)| = |g(1 - \Delta)|$. The dissipation is quite small for small α or Δ. In all cases $|g| \leq 1$, which means the method is numerically stable and has no Courant condition (recall our analysis is for $\Delta < 1$, but $\Delta > 1$ is simply handled by basing the interpolant off a a position shifted by more than one gridpoint). Also, $g(k = 0) = 1$, indicating that the mean value of f is unchanged. That is, the "mass" $\int dx\ f$ is *globally* conserved (although in general it is not *locally*).

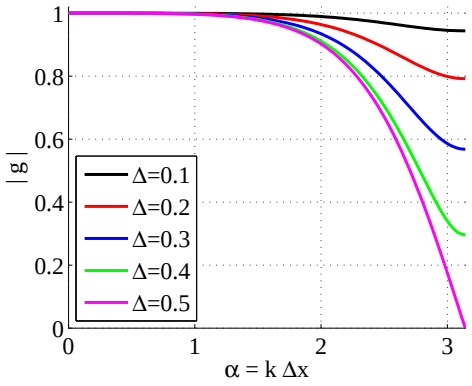

Figure 3. Magnitude of numerical amplification factor g for advection by cubic spline interpolation, Eq. (27). The same plot applies for either choice of $\sigma = \text{sign}\, v$, for $\alpha \to -\alpha$, and for $\Delta \to 1-\Delta$.

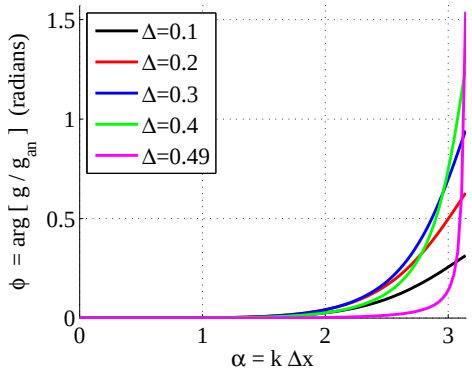

Figure 4. Numerical phase error $\phi = \arg[g/g_{\text{an}}]$ in one timestep, for $\sigma = \text{sign}\, v = 1$ for advection by cubic spline interpolation, Eq. (27). Note that $\phi(-\alpha) = -\phi(\alpha)$, $\phi(\sigma = -1) = -\phi(\sigma = 1)$, and $\phi(1-\Delta) = -\phi(\Delta)$.

Figure 4 plots the phase error ϕ, and several anti-symmetry relations for ϕ are given in the caption. The error is quite small away from $\alpha = \pi$, so that as long as the features being advected are well-resolved their dispersion is accurate. The figure is repeated on a logarithmic scale in Fig. 5. It is interesting that ϕ assumes an almost universal form when α is not too large and Δ departs from 1/2.

So far we have described the solution for interior points and neglected boundary conditions (BCs). ELVIS uses periodic BCs in x, even though we frequently study non-periodic problems like SRS. Following Fig. 1, the periodicity domain in x is x_L to x_R, with $f \equiv 0$ in the exterior "moat" regions where transverse e/m waves propagate in vacuum to the final boundaries $x = 0, L$. To make the problem effectively periodic, we use finite density profiles and large Krook rates in boundary regions. Periodic BCs are both easy to implement and maintain global number conservation. Early work with ELVIS collected escaping particles on boundary plates [23], but this proved impractical due to large localized fields that de-

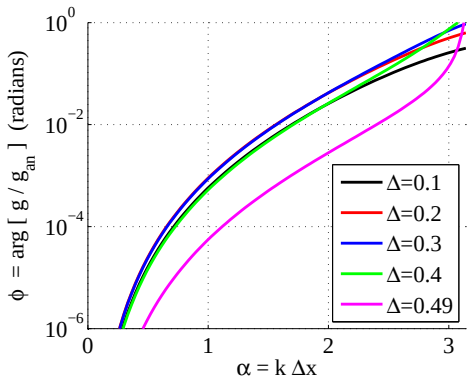

Figure 5. Figure 4 on a logarithmic scale.

veloped. Particle re-emission from a thermal bath is another possibility. The momentum shift uses open boundaries, where we assume $f = 0$ outside the finite p_x grid. This leads to a loss of particles, and can be remedied by replenishing from a thermal Maxwellian bath after the p_x shift. In this chapter, no bath is used in the electrostatic problems (but number conservation is still excellent, see Fig. 8), while it is used in the SRS runs.

2.4. Krook Operator

We seek a Krook time-advance operator $\tilde{U}_K$ that solves $\partial_t f = \nu_K(n\hat{f}_0 - f)$ to at least second-order accuracy. This equation leaves the density n unchanged, as is readily seen by integrating it over p_x. We can thus use the exact solution to this linear equation:

$$f(t) = f(0)e^{-\nu_K t} + n\hat{f}_0(1 - e^{-\nu_K t}). \tag{28}$$

It is important that distributions, such as $\hat{f}_0$, be normalized numerically and not analytically. That is, $\int dp_x\, \hat{f}_0$, as computed on the discrete p_x grid and with the method used to numerically compute density, must be unity. Otherwise, $\tilde{U}_K$ will steadily change the number density over time. The same comment applies to setting up f to have a desired initial density. For finite-geometry runs, we use a large ν_{Ks} in "damping regions" (see Fig. 1) at the edges to absorb plasma waves generated inside the plasma (e.g., by SRS) and to damp fluctuations generated in the density profile ramps.

2.5. Solving for E_x

The longitudinal electric field E_x is found directly from ρ and Gauss' law, Eq. (2), and not via the potential ϕ, although we frequently find ϕ for diagnostic purposes. We find E_x by either a Fourier or finite-difference method. We use the Fourier method for essentially periodic problems, such as a wave over one or several wavelengths, and the finite-difference method for finite problems like SRS (the gradual evolution of wave envelopes over many wavelengths). In either case, boundary conditions (BCs) must also be specified. These and various solution methods are discussed on pp. 75-79 and App. D of Ref. [34].

For a periodic system from $x = 0$ to L, we have $E_x(0) = E_x(L)$. Integrating Gauss' law from 0 to L gives $E_x(L) - E_x(0) = Q$ where $Q = \int dx\ \rho$ is the total charge in the system. Q must be 0 for E_x periodic, so we can only apply periodic BCs for systems with no net charge. For periodic BCs we must impose an additional condition to set the absolute level of E_x. One choice is to eliminate DC fields by shifting E_x so it has zero average; this is also called a "short-circuit" BC . It is equivalent to demanding ϕ be periodic, which implies E_x has zero average (analogous to the relation between ρ and E_x for periodic BCs).

Our finite-difference solution of Gauss' law involves finding E_x at fictitious half gridpoints and then averaging to find E_x at full gridpoints. In particular,

$$E_{x,j+1/2} - E_{x,j-1/2} = \Delta x\, \rho_j, \qquad E_{x,j} = \frac{1}{2}(E_{x,j+1/2} + E_{x,j-1/2}). \tag{29}$$

This method is equivalent to finding ϕ with the usual 3-point centered stencil for ϕ'' and then E_x by a centered difference. Our method eliminates the need to solve a tridiagonal system.

To find the accuracy of this method, consider interior points (neglect boundaries), and for full gridpoints let $E_{x,j} = \tilde{E}_{x,j} + e_j$ where $E_{x,j}$ is our numerical approximation, $\tilde{E}_x(x)$ is the true E_x, and $e(x)$ is the error ($\tilde{E}_x$ and e are continuous functions of x). Assuming $\rho_{x,j}$ is exact, we find by Taylor expanding that $e_j = (\Delta x^2/12)\partial_{xx}\tilde{E}_{x,j}$. The method is thus second-order accurate in Δx. It is also highly localized in space. For a unit impulse $\rho_j = \delta_{jk}$, we have $E_{x,j} = (0, \Delta x/2, \Delta x)$ for $(j \le k-1, j = k, j \ge k+1)$. The full change in E_x thus occurs over a few gridpoints.

Our Fourier method for finding E_x, appropriate for periodic systems, utilizes "exact" differentiation in wavenumber space. That is, with the Fourier transform $\hat{f}(k) = \int dx\ e^{-ikx} f(x)$ for the field f, Gauss' law gives $ik\hat{E}_x = \hat{\rho}$ for $k \neq 0$. $\hat{E}_x(k=0)$ is the average value of E_x, which must be determined by BCs. ϕ is simply found from $\hat{E}_x = -ik\hat{\phi}$. This "exact" approach is spectrally accurate but highly nonlocal, in that E_x at one x is influenced by ρ at all x (with the influence dropping off weakly). This is an effective approach to intrinsically periodic problems, but undesirable for, say, envelope evolution like in SRS. A more spatially local differentiation operator than ik can be used, at the expense of spectral accuracy, but we do not adopt one. See App. E of Ref. [34] for an illuminating discussion of these issues.

2.6. Advance of transverse fields $E^{\pm}, v_{ys}$

We now turn to the time advance of the transverse fields $E^{\pm}$ and v_{ys}, performed by the operators M_1 and Y_1. For simplicity we consider only electrons ($v_{ys} \to v_{ye}$). We must advance $E^{\pm}$ from timestep $t_{n-1/2}$ to $t_{n+1/2}$, and v_{ye} from t_n to t_{n+1}. The relevant PDEs in ELVIS units are

$$(\partial_t \pm \partial_x)E^{\pm} = n_e v_{ye}, \tag{30}$$

$$\partial_t v_{ye} = -\frac{1}{2}(E^+ + E^-). \tag{31}$$

n_e is held constant at t_n, as is appropriate for our overall timestep. To obtain the dispersion relation for the continuous PDEs, first verify $(\partial_{tt} - \partial_{xx})E_y = n_e \partial_t v_{ye} = -n_e E_y$ using E^+

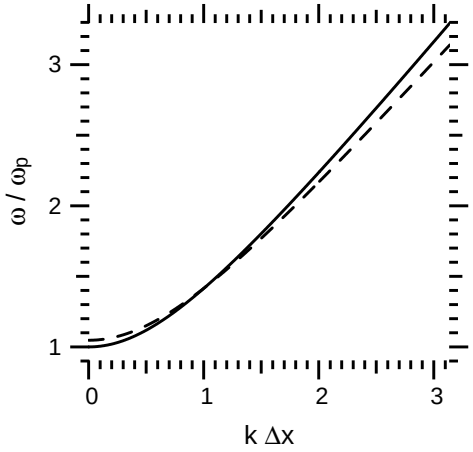

Figure 6. Dispersion relation for transverse dynamics. The solid curve is the exact, continuous result $\omega_{\rm em}^2 = \omega_p^2 + c^2k^2$. The dashed curve is the numerical result $\omega_{\rm num}$, Eq. (38), for $a = \omega_p \Delta t = 1$.

and E^- (it is useful to factorize $\partial_{tt} - \partial_{xx} = (\partial_t + \partial_x)(\partial_t - \partial_x)$). Then Fourier analyzing by assuming $\exp i(kx - \omega t)$ space-time variation for all fields, we find in physical units $\omega = \omega_{\rm em} \equiv \omega_p[1 + (kd_e)^2]^{1/2}$ with $d_e \equiv c/\omega_p$. This is the usual dispersion relation of light waves in a cold plasma.

For the discrete time advance, we shift $E^\pm$ along the appropriate vacuum characteristics ($x = x_0 \pm ct$) by exactly one gridpoint. This requires $\Delta x = c\Delta t$, and this constraint obtains whenever transverse fields are used. For $J_y = 0$, this gives the exact $E^\pm$. The source J_y is evaluated at the midpoint of the characteristic. v_{ye} is advanced by the midpoint rule. Thus,

$$E_j^{+,n+1/2} = E_{j-1}^{+,n-1/2} + n_{e,j-1/2}^n v_{ye,j-1/2}^n \Delta t, \tag{32}$$

$$E_j^{-,n+1/2} = E_{j+1}^{-,n-1/2} + n_{e,j+1/2}^n v_{ye,j+1/2}^n \Delta t, \tag{33}$$

$$v_{ye,j}^{n+1} = v_{ye,j}^n - (\Delta t/2)(E_j^{+,n+1/2} + E_j^{-,n+1/2}), \tag{34}$$

$$v_{y,j-1/2}^n = (1/2)(v_{j-1}^n + v_j^n). \tag{35}$$

We find the numerical dispersion and dissipation of this method via a standard von Neumann analysis. Assume all fields vary as $\exp i(kx - \omega t)$ on the discrete grids, and write them as

$$(E^+, E^-, v_{ye})_j^n = (\mathcal{E}^+, \mathcal{E}^-, V) \exp i(kj\Delta x - \omega_{\rm num} n\Delta t). \tag{36}$$

We insert these into the discrete time-advance equations, solve for $\mathcal{E}^\pm$ in terms of V, and then substitute into Eq. (34) to obtain the numerical dispersion relation

$$D = 0 = a^2 + (a^2 - 4)\cos k\Delta x + 4\cos \omega_{\rm num}\Delta t; \qquad a \equiv \omega_p \Delta t. \tag{37}$$

This is readily solved for $\omega_{\rm num}$:

$$\omega_{\rm num}\Delta t = \arccos\left[-a^2/4 + (1 - a^2/4)\cos akd_e\right]. \tag{38}$$

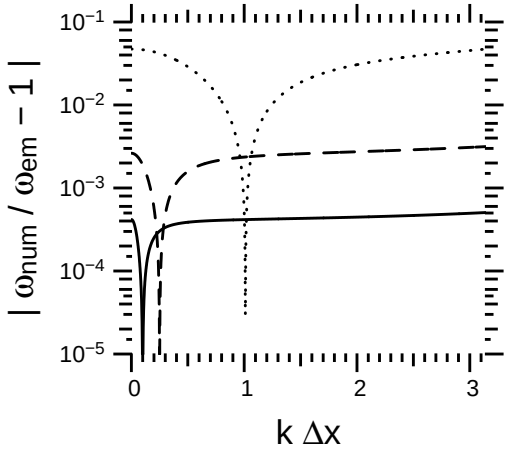

Figure 7. Phase error $|\omega_{\rm num}/\omega_{\rm em}-1|$ of the numerical time advance for transverse dynamics. The solid, dashed, and dotted curves are for $a=\omega_p\Delta t=0.1$, 0.25, and 1, respectively.

We imposed $\Delta x = c\Delta t$. For real k, $\omega_{\rm num}$ is real (no numerical dissipation) as long as $|\cos\omega_{\rm num}\Delta t|\le 1$. This obtains as long as $\omega_p\Delta t\le 2$. The algorithm has no dissipation if this condition is met.

$\omega_{\rm num}(k)$ is shown in Fig. 6 for $\omega_p\Delta t=1$. Even for this rather large timestep the agreement is quite good. We only need to consider $|k|\le\pi/\Delta x$ (the Nyquist value); since $D(-k)=D(k)$ we only plot $k>0$. Taylor expanding Eq. (38) for Δt small, we find

$$\frac{\omega_{\rm num}}{\omega_{\rm em}}\approx 1+\frac{1}{24}\frac{1-(kd_e)^2}{1+(kd_e)^2}a^2+O(a^4). \tag{39}$$

We thus recover the correct continuous light-wave dispersion relation for small a. Figure 7 plots the dispersion error. Note from Fig. 6 that, for $a=1$, $\omega_{\rm num}=\omega_{\rm em}$ for $k\Delta x\approx 1$. There is generally a k where the phase error is zero, corresponding to the dips in Fig. 7. We see from Eq. (39) that the $O(a^2)$ error vanishes for $kd_e=1$ (but the $O(a^4)$ error does not; $kd_e=0$ is thus approximately where $\omega_{\rm num}=\omega_{\rm em}$). $kd_e=1$ corresponds to $k\Delta x=a$, which is about where the dips in Fig. 7 occur.

The discretization (or truncation) error of the transverse time advance is $O(a^2)$. To see this, we can form the residual R (which is identically zero) for the time advance of E^+ (an analogous calculation applies for E^-):

$$R^n_{j-1/2}\equiv E_j^{+,n+1/2}-E_{j-1}^{+,n-1/2}-(N\Delta t/2)(v^n_{ye,j-1}+v^n_{ye,j}). \tag{40}$$

We use $N=n^n_{e,j-1/2}$ and neglect its variation in space and time (which is of secondary importance for light waves). Write $E^+=\tilde E^+ + e_+$ and $v_{ye}=\tilde v_{ye}+e_v$ where $\tilde E^+,\tilde v_{ye}$ are the true fields and e_+,e_v the error fields (both true and error fields are continuous functions, and not just known on the discrete grid). Let $R^n_{j-1/2}=\tilde R+R_e$ where $\tilde R$ and R_e contain true and error fields, respectively. Taylor expanding yields

$$\tilde R=\left[(\partial_t+\partial_x)\tilde E^+ - N\tilde v_{ye}\right]\Delta t+\left[(\partial_t+\partial_x)^3\tilde E^+ - 3N\partial_{xx}\tilde v_{ye}\right]\Delta t^3+O(\Delta t^5). \tag{41}$$

The same expression, with true fields replaced by error fields, obtains for R_e. All fields are evaluated at t_n and $x_{j-1/2}$, so we suppress the index labels. The continuous PDEs Eqs. (30-31) make the $O(\Delta t)$ term in $\tilde{R}$ zero. Thus, the total R contains an $O(\Delta t)$ combination of error fields, which must balance an $O(\Delta t^3)$ combination of true fields. The error fields are therefore $O(\Delta t^2)$. Note that for no plasma ($N = 0$), Eq. (30) annihilates the $(\partial_t + \partial_x)^3$ operator, so that $\tilde{R}$ would be $O(\Delta t^5)$. In fact $\tilde{R} = 0$ for $N = 0$ since the $E^{\pm}$ advance is exact in this case. An analysis of the v_{ye} time advance, analogous to Eq. (29) for $E_{x,n+1/2}$, shows it entails $O(\Delta t)$ error fields balancing $O(\Delta t^3)$ true fields, which again is consistent with $O(\Delta t^2)$ errors.

3. Electrostatic application: Langmuir-wave dispersion

As a demonstration of ELVIS on an electrostatic problem (no transverse fields), we choose the evolution of a Langmuir wave (LW) from an initial density perturbation. This illustrates the linear and nonlinear (particle trapping) physics of plasma waves. In addition, the so-called "recurrence problem" of Eulerian Vlasov codes is revealed (see below). The domain is spatially periodic, of length one wavelength $\lambda = 2\pi/k$, and E_x is found by the Fourier method with short-circuit BCs. Ions form a uniform immobile background, and $\nu_K = 0$ (no Krook operator). The electron distribution initial condition (IC) is

$$f_e(t=0) = f_0(p_x)(1+\varepsilon\sin(kx)). \tag{42}$$

f_0 is an equilibrium 1D distribution, either

$$f_0^{NR} = \frac{n_0}{p_{Te}(2\pi)^{1/2}} e^{-p_x^2/2p_{Te}^2} \qquad \text{or} \tag{43}$$

$$f_0^{R} = \frac{n_0}{2\mu m_e c K_2(\mu)}(1+w_x)e^{-w_x}. \tag{44}$$

$p_{Te} \equiv m_e v_{Te}$ with $v_{Te} \equiv [T_e/m_e]^{1/2}$ the electron thermal speed, $\mu \equiv m_e c^2/T_e$, K_2 is the modified Bessel function of the second kind and order two, and $w_x \equiv \mu[1+u_x^2]^{1/2}$. f_0^{NR} and f_0^R are used, respectively, for non-relativistic and relativistic runs. The only other change between the two modes is the formula for γ_x in the advective $v_x\partial_x$ term in the Vlasov equation. $f_0^R = \int du_y du_z\, f_J$ is an ad-hoc 1D reduction of the 3D Jüttner, or relativistic Maxwellian, distribution f_J:

$$f_J = \frac{n_0\mu}{4\pi(m_e c)^3 K_2(\mu)} e^{-\mu\gamma}. \tag{45}$$

$\gamma = [1+u^2]^{1/2}$ is the full, 3D Lorentz factor.

The IC Eq. (42) produces a standing wave, or two traveling waves of amplitude $\delta n = n_0\varepsilon/2$ with phase velocities $\pm v_p$ where $v_p \equiv \omega/k$ and ω is the normal-mode real frequency corresponding to k (there is transient behavior associated with strongly-damped roots to the dispersion relation, which vanish after $\sim$ one plasma period). As long as the trapping regions in velocity, $\pm(v_p \pm v_{tr})$, of the two waves are separate, the dynamics are essentially that of two non-interacting traveling waves. $v_{tr} = 2(\omega_p/k)(\delta n/n_0)^{1/2}$ is the *half*-width of phase space vortex formed by one traveling wave.

The non-relativistic linear theory of LWs is well-known, although the relativistic theory, using Eq. (45), has recently been the subject of renewed interest [35]. We merely state the non-relativistic dispersion relation $\varepsilon_{NR} = 0$ (see Ref. [35] for details) where the dielectric ε_{NR} is

$$\varepsilon_{NR} \equiv 1 - \frac{1}{2(k\lambda_D)^2} Z'(\zeta) \qquad \zeta \equiv \frac{v_p^C}{v_{Te}\sqrt{2}}. \tag{46}$$

$\lambda_D = v_{Te}/\omega_p$ is the Debye length, Z is the plasma dispersion function, and $Z'(\zeta) = dZ/d\zeta$. $v_p^C = \omega^C/k$ is the complex phase velocity, computed for real k but complex ω^C. We usually find ω^C for real k that satisfies the dispersion relation, and take $\omega = \mathrm{Re}\ \omega^C$ as the real frequency; the context should make clear whether we mean the real or complex ω. The relativistic Landau damping rate was calculated analytically in Ref. [35], and found to be significantly less than the non-relativistic value for high temperatures. This fact, along with the complete vanishing of Landau damping for super-luminal phase velocities ($v_p > c$), was found earlier by a quantum statistical-mechanics calculation [36].

The recurrence problem in Eulerian Vlasov codes is a sign of filamentation, or the transport of structure to finer velocity scales as time progresses. For the non-relativistic IC Eq. (42), the force-free Vlasov equation $(\partial_t + v_x\partial_x) f = 0$ can be solved along characteristics to give $f = f_0(v_x)[1 + \varepsilon \sin k(x - v_x t)]$. The velocity "wavenumber" kt grows with time. The exact density n decays rapidly toward n_0 due to phase mixing, and is

$$n/n_0 = 1 + \varepsilon \sin(kx) \exp[-(v_T kt)^2/2]. \tag{47}$$

On a fixed v_x grid, the evolution is distorted once kt approaches the grid spacing. In particular, on a uniform grid $v_{x,j} = j\Delta v$, $ktv_{x,j} = 2\pi jM$ (M integer) whenever $t = Mt_{\mathrm{rec}}$ where $t_{\mathrm{rec}} \equiv \lambda/\Delta v$ is the recurrence time. At these times, $\sin k(x - v_{x,j}t) = \sin kx$ on the discrete v grid, and the numerical density equals n_0.

As shown in Fig. 9, recurrence occurs for periodic problems with forces included, even when the initial wave has Landau damped to a small fraction of its initial amplitude by t_{rec}. This is despite the weak numerical damping of high-k modes in cubic spline advection (see Fig. 3), which is ineffective over the time it takes structure to "march up" to the grid spacing. We do not take any special action to prevent filamentation or recurrence, although techniques which artificially damp fine-scale velocity structure have been used by others, e.g. including a numerical hyper-viscosity $\partial_v^{(4)} f$ [37, 38]. Instead, numerical parameters are chosen so t_{rec} exceeds times of interest, such as the time for Landau damping or trapping to occur in the initial-value problems of this section, or the decoherence time of SRS (taken to be an inverse of the growth rate) in laser-plasma problems. We have seen no signs of recurrence in SRS problems.

O'Neil [10] studied analytically the initial-value problem for Langmuir waves, which we have just described. He solved for particle orbits in a single traveling wave of constant amplitude, including both those trapped in the wave potential well and those that are not (the so-called passing particles). From this the rate of wave energy loss is obtained, which shows the collisionless (Landau) damping rate oscillates and decays over several bounce periods $\tau_B \equiv 2\pi\omega_p^{-1}(n_0/\delta n)^{1/2}$ of the deeply trapped particles. This reduction in Landau damping leads to the "inflation," or increase, of SRS above linear predictions [17, 18]. Later, Morales and O'Neil analyzed the nonlinear frequency downshift in a similar way

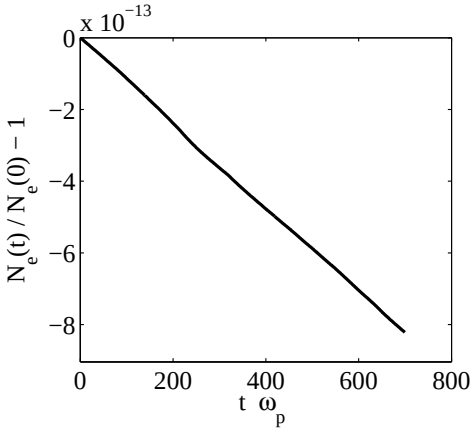

Figure 8. Change in total electron number for non-relativistic Langmuir-wave run NR1 with $k\lambda_D = 0.3$ and $\varepsilon = 10^{-4}$.

[11]. Dewar [12] calculated the frequency shift for both a suddenly-created wave (like in the initial value problem) and an adiabatically driven one. This shift may act as a saturation mechanism for SRS, and leads to rich multi-D physics [15, 39, 16, 13].

We first present a non-relativistic problem, which we call run NR1, with $k\lambda_D = 0.3$ and $\varepsilon = 10^{-4}$. For the non-relativistic case, the background density and temperature scale out of the problem. The linear, analytic, non-relativistic dispersion relation is $\varepsilon_{NR} = 0$ with ε_{NR} from Eq. (46). For $k\lambda_D = 0.3$, this gives $\omega = 1.16\omega_p$, $v_p = \omega/k = 3.87v_{Te}$, and an energy damping rate $\nu = 0.0252\omega_p$. We use numerical parameters $\Delta x = \lambda/32$, $\Delta t = \omega_p^{-1}/32$, and a momentum grid extending to $\pm 8p_{Te}$ with $\Delta p/p_{Te} = 16/256 = 0.0625$. We intentionally do not use an excessively fine resolution, to show that high accuracy can still be achieved. The recurrence time is $t_{\rm rec} = 335\omega_p^{-1}$. Particle number conservation, shown in Fig. 8, is excellent, even though open boundaries in p_x are used (recall from Sec. 2.3. that cubic spline interpolation with periodic BCs, which we use in x, conserves global number). The total wall runtime on one Opteron CPU was about 40 ns per advance of each phase-space cell in the distribution (grand total of $N_t N_x N_p$); this is typical of small electrostatic runs, but is usually several times larger for SRS problems.

The kinetic, electrostatic, and total energies W_k, W_E, W_t, summed over the simulation domain, are defined as

$$W_k \equiv \int dx dp_x\, w_k f; \qquad W_E \equiv \int dx \frac{\varepsilon_0}{2} E_x^2; \qquad W_t \equiv W_k + W_E. \tag{48}$$

w_k is the single-particle kinetic energy: $w_k = m_e v_x^2/2$ or $m_e c^2(\gamma_x - 1)$ for non-relativistic and relativistic dynamics, respectively. Figure 9 plots W_E and the change in W_k for run NR1, averaged over one plasma period. W_E decays as the wave Landau damps, and the lost field energy appears as particle kinetic energy. This process reverses around $t_{\rm rec}$, and the wave energy grows until reaching about half its initial value around $t = 400\omega_p^{-1}$. Imperfect reconstruction of $W_E(t=0)$ is due to either numerical dissipation or the inclusion of forces. Figure 10 displays W_E on a log scale, from which the energy damping rate is found by fitting a line between $t\omega_p = 25 - 230$ to be $\nu_{\rm num} = 0.0251\omega_p$ (which is the slope of the straight

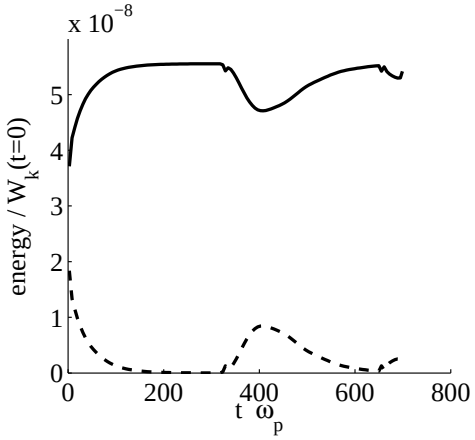

Figure 9. Change in kinetic energy $W_k(t) - W_k(0)$ (solid curve), and electrostatic energy W_E (dashed curve), for run `NR1`. The rebound of W_E, peaking at $t \approx 400\omega_p^{-1}$, is due to recurrence ($t_{\rm rec} \approx 335\omega_p^{-1}$).

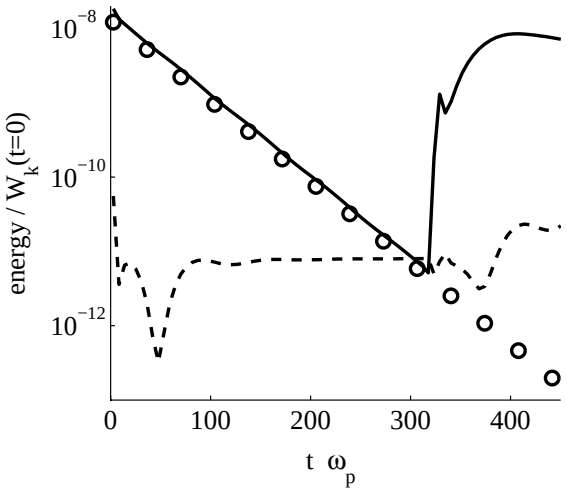

Figure 10. Electrostatic energy W_E (solid curve), and change in total energy W_t (dashed curve), for run `NR1`. The straight line of open circles corresponds to linear energy damping $\exp[-\nu_{\rm num} t]$ with $\nu_{\rm num} = 0.0251\omega_p$.

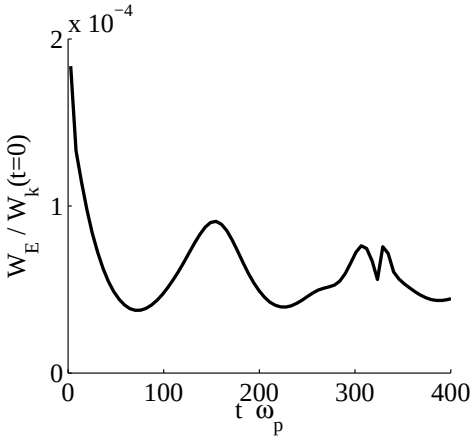

Figure 11. Electrostatic energy W_E for run NR2. The initial density perturbation is $\varepsilon = 0.01$, giving an initial bounce period of $\tau_B = 88.6\omega_p^{-1}$. Rebound of the wave energy W_E occurs later than O'Neil's result of $\approx 1.25\tau_B = 111\omega_p^{-1}$ since the initial linear damping decreases δn and increases τ_B. The spike near $300\omega_p^{-1}$ is related to recurrence.

line of open circles). This compares very well with the analytic value $\nu_{\text{anal}} = 0.0252\omega_p$. In addition, the change in total energy W_t is shown in Fig. 10 to be much less than W_E and the change in W_k.

To demonstrate trapping nonlinearity, we performed the run NR2 which differs from NR1 only in that $\varepsilon = 0.01$ instead of 10^{-4}. This gives a traveling wave amplitude of $\delta n = 0.005 n_0$, a trapping half-width of $v_{tr}/v_{Te} = 0.471$, and an initial bounce period $\tau_B = 88.6\omega_p^{-1}$. After initially decaying, the wave energy rebounds and reaches a second peak near the time $150\omega_p^{-1}$ (see Fig. 11). According to the O'Neil theory, the wave should reach its second peak around $1.25\tau_B$, which is about $111\omega_p^{-1}$ using the initial τ_B. However, this calculation assumes a fixed wave amplitude. Since the wave initially damps, it takes slightly longer for trapping to occur. Vortex formation in phase space due to trapping is shown in Fig. 12, where the distribution f_e is plotted at $t = 122\omega_p^{-1}$, after the wave has started to rebound. The vortex is centered near the linear phase velocity $v_p = 3.87 v_{Te}$ of the right-moving traveling wave. Although it is possible to use higher resolution and display fine details of f_e, we obtain accurate results with this relatively coarse meshing.

We consider now a relativistic run, Rel1, which is analogous to NR1 ($k\lambda_D = 0.3$, $\varepsilon = 10^{-4}$) except the relativistic IC and Lorentz factor γ_x are used. We also must specify T_e (more precisely, $T_e/m_e c^2$), as this does not scale out of the relativistic problem as it does in the non-relativistic case. To demonstrate the relativistic reduction of Landau damping, we take $T_e = 17.033$ keV ($\mu = m_e c^2/T_e = 30$). The numerical parameters are $\Delta x = \lambda/64$, $\Delta t = 0.0909\omega_p^{-1}$, p_x runs from $\pm 1.54 m_e c$, and $\Delta p/m_e c = 2 \cdot 1.54/512 = 0.00602$. The recurrence time is $t_{\text{rec}} \approx 635\omega_p^{-1}$, beyond the run end. Figure 13 depicts the field energy W_E, which decays at approximately the rate $\nu_{\text{num}} = 0.00258\omega_p$. The relativistic, analytic theory of Ref. [35] gives a linear energy damping rate of $\nu_{\text{anal}} = 0.00316\omega_p$, which is 22% larger than the numerical result. The discrepency may be due to the reduction of the Vlasov equation or distribution function from 3D to 1D in momentum. This is complicated rela-

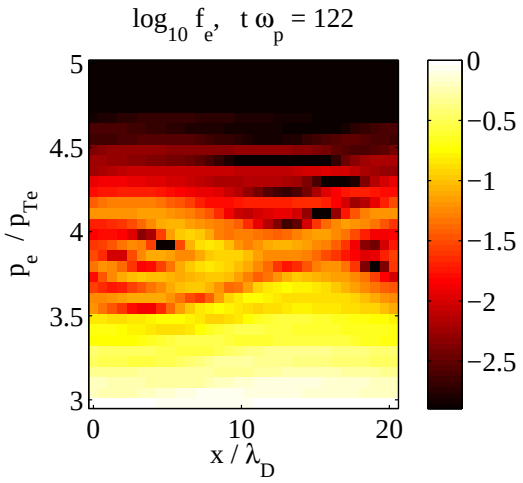

Figure 12. Electron distribution f_e for run NR2 at the time $122\omega_p^{-1}$, after the wave energy has started to rebound. The phase-space vortex is due to electron trapping and is centered on the right-moving traveling wave phase velocity of $\omega/k = 3.87v_{Te}$.

tivistically by the fact that the Lorentz factor γ, which appears in both the Vlasov equation and the Jüttner distribution, couples all three momentum components in a way that does not factor. Our treatment of the advective $v_x\partial_x f$ term in particular may need refinement: the use in ELVIS of $v_x/c = u_x/\gamma_x$ with $\gamma_x = [1+u_x^2]^{1/2}$ entails treating the distribution as cold in the transverse momenta. Nonetheless, the two relativistic damping rates (numerical and analytic) qualitatvely agree, in that they are much smaller than the non-relativistic result of $0.025\omega_p$.

4. Application to Raman scattering

This section presents simulations of stimulated Raman scattering (SRS) with ELVIS. In SRS, a pump light wave, which we label mode 0 (such as a laser, contained in E^+), decays into a scattered light wave (mode 1, contained in E^-) and a Langmuir wave (mode 2). This resonant, three-wave process satisfies the phase matching conditions $\omega_0 = \omega_1 + \omega_2$ and $\vec{k}_0 = \vec{k}_1 + \vec{k}_2$, which reflect conservation of energy and momentum, respectively. We focus on backscatter in ELVIS geometry, where $\vec{k}_i = k_i\hat{x}$, $k_0, k_2 > 0$, and $k_1 < 0$. We use the finite geometry illustrated in Fig. 1, with a large Krook rate ν_K at the density ramp-ups to prevent fluctuations. A pump laser is incident from the left edge, with intensity I_{0L} (we use subscript L and R to denote quantities at the left and right edge). Due to the low numerical noise in Eulerian Vlasov codes like ELVIS, SRS generally does not develop "spontaneously" from this system. To initiate SRS, we include a seed scattered light wave on the right edge with intensity I_{1R} and wavelength λ_{1s}.

We first present kinetic inflation of SRS and the development of and scattering off electron acoustic waves in Sec. 4.1. The suppression of trapping by a Krook operator, intended to mimic transverse speckle loss, is examined in Sec. 4.2. Section 4.3 shows the insensitiv-

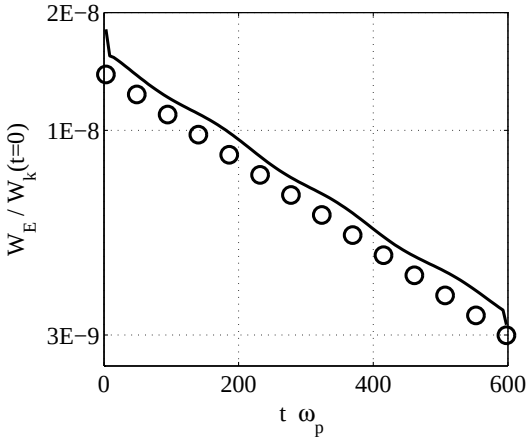

Figure 13. Electrostatic energy W_E for relativistic run `Rel1` (log scale), with initial density perturbation $\varepsilon = 10^{-4}$ as in run `NR1`. The straight line of open circles corresponds to linear energy damping $\exp[-\nu_{\rm num} t]$ with $\nu_{\rm num} = 0.00258\omega_p$.

ity of the SRS reflectivity to the use of a Gaussian broadband (instead of monochromatic) scattered-light seed. Ref. [18] covers the material of Sec. 4.1 in detail, and Ref. [40] presents aspects of all three sections.

4.1. Kinetic inflation and electron acoustic scatter (no Krook operator)

As a first example, we demonstrate the kinetic inflation, or enhancement, of SRS due to electron trapping and the resulting decrease in Landau damping [17, 18]. For the run series "`SRS1`", we take a laser with vacuum wavelength $\lambda_0 = 527$ nm (frequency-doubled light for Nd:glass lasers), a homogeneous plasma with $n_e/n_{cr} = 0.025$ and $T_e = 500$ eV ($n_{cr} \equiv \varepsilon_0 m_e \omega_0^2/e^2$ is the critical density where $\omega_p = \omega_0$). These parameters were also studied in Ref. [18] and are motivated by single hot spot experiments done at the Trident laser facility [41, 42], which explored SRS from a single laser speckle. ICF hohlraum conditions where SRS is expected to be most active are hotter and denser ($T_e \sim 2$ keV, $n_e/n_{cr} \sim 0.1$). Both conditions entail similar values of $k_2\lambda_D$, and the same qualitative features were demonstrated for hohlraum conditions in Ref. [18] . The ions are immobile, and for now $\nu_K = 0$ outside of the ramp regions. This gives a Krook-free central flattop of length of length 75.4 μm surrounded by 9.8 μm of "overhead" (ramps and moats) on each side.

The linear, collisionless, kinetic dispersion relation for SRS was found by Drake et al. [43]. For the `SRS1` parameters, the temporal most unstable mode for weak pump intensity obtains for $k_2\lambda_D = 0.352$ (which has an amplitude Landau damping rate of $\nu_2 = 0.0354\omega_p$), or $\lambda_1 = 653$ nm. We use $\lambda_{1s} = 653.4$ nm ($\omega_{1s}/\omega_p = 5.10$) and $I_{1R} = 10^{-5} I_{0L}$. The spatial grid spacing is $\Delta x = \lambda_2/20$ (recall $\Delta t = \Delta x/c$) with λ_2 given by matching with λ_0 and λ_{1s}. For the velocity grid we use $\Delta v < v_{tr,s}/4$ where $v_{tr,s}$ is the trapping width v_{tr} calculated for the beating of the pump and seed waves. That is, we resolve phase-space islands even if there were no SRS amplification.

The instantaneous SRS reflectivity is $R(t) \equiv I_{1L}(t)/I_{0L}$ where I_{1L} is the reflected (left-

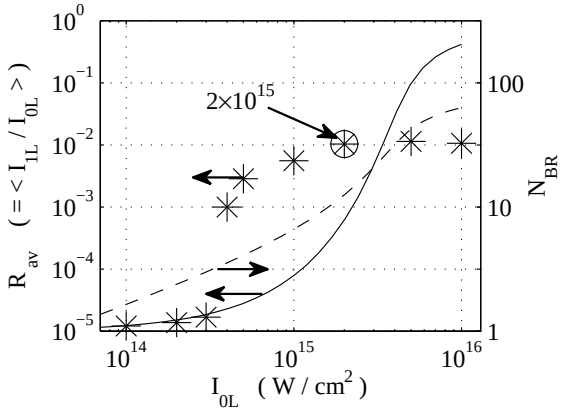

Figure 14. Solid curve: SRS reflectivity for run series `SRS1`, calculated in the convective steady state with pump depletion, Eq. (52). Stars: time-averaged reflectivity $R_{\rm av}$ for ELVIS runs. The specific run `SRS1_2`, with $I_{0L} = 2 \times 10^{15}$ W/cm^2, is circled. Dashed curve: bounce number N_{BR} for an electron that crosses the full domain, see Eq. (54).

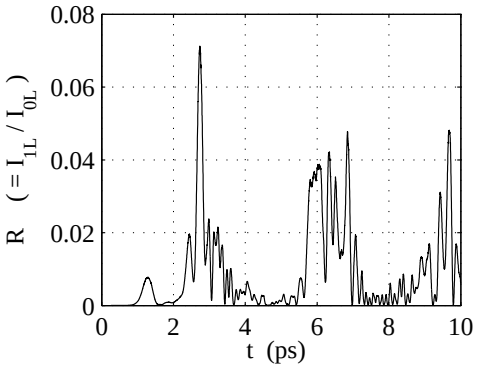

Figure 15. Instantaneous reflectivity $R(t)$ for run `SRS1_2` ($I_{0L} = 2 \times 10^{15}$ W/cm^2). The time-average is $R_{\rm av} = 0.0103$.

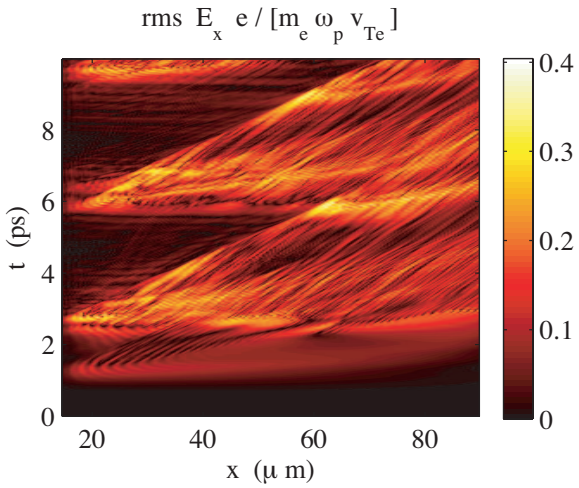

Figure 16. Envelope (root mean square) of the electrostatic field E_x for run SRS1_2, neglecting the edge overhead regions.

moving) light intensity at the left edge. $I_i = (\varepsilon_0/2)|v_{gi}|E_i^2$ is the intensity of light wave i, with $|v_{gi}|/c = [1-\omega_p^2/\omega_i^2]^{1/2}$ the magnitude of the group velocity and $v_{os,i} = eE_i/m_e\omega_i$ the electron oscillation speed. These quantities are all found in plasma, not vacuum. Also, the undamped SRS amplitude growth rate is

$$\gamma_0 = k_2 v_{os,0} \frac{\omega_p}{4[\omega_1\omega_2]^{1/2}}. \tag{49}$$

Figure 14 displays the time-averaged reflectivity $R_{\rm av} = \langle R(t)\rangle$ for the run series SRS1. All runs were below the homogeneous absolute instability threshold $I_{0a} = 2.98\times10^{16}$ W/cm^2 for undamped light waves, which gives $\gamma_0 = \gamma_{0a} \equiv (1/2)|v_{g1}/v_{g2}|^{1/2}\nu_2$, with v_{g2} the LW group velocity. Coupled-mode theory thus predicts SRS approaches a temporal steady state where the seed light wave is convectively amplified across the box.

The steady state can be solved analytically for a three-wave model that includes depletion of the pump laser but no light-wave damping, and neglects LW advection compared to damping (the strong damping limit) [44]. This is valid for $I_{0L} \ll I_{0a}$. The scattered light wave in this limit satisfies

$$\frac{d\hat{I}_1}{dx} = -\frac{G}{L}\hat{I}_0\hat{I}_1, \tag{50}$$

where $\hat{I}_0 = I_0(x)/I_{0L}$, $\hat{I}_1 = I_1(x)/I_{1R}$, and $I_0/\omega_0 - I_1/\omega_1 =$ constant. This last expression of action-flux conservation is a spatial version of the Manley-Rowe relations. L is the length of the gain region, and the intensity gain exponent G is

$$G \equiv \frac{L\lambda_{1p}}{\lambda_2^2}\left[1-\frac{n_e}{n_{cr}}\right]^{-1/2} \mathrm{Im}\left[\frac{\chi}{1+\chi}\right]\frac{I_{0L}\lambda_0^2}{871\times10^{15}\,\mathrm{W}\,\mu\mathrm{m}^2/\mathrm{cm}^2}. \tag{51}$$

λ_{1p} is the scattered light wavelength in the plasma. $\chi(k_2,\omega_2) = \varepsilon_{NR} - 1$ is the electron susceptibility, where the dielectric ε_{NR} is given in Eq. (46). k_2 and ω_2 are given by the

beating of the chosen pump and scattered light waves. The resulting reflectivity is

$$\tilde{R}(1-\tilde{R}+\tilde{s}) = \tilde{s}\exp\left[G(1-\tilde{R})\right] \tag{52}$$

with $\tilde{R} = (\omega_0/\omega_1)R$ and $\tilde{s} = (\omega_0/\omega_1)I_{1R}/I_{0L}$.

For small pump intensities, Fig. 14 shows the ELVIS reflectivities are small and in agreement with the analytic coupled-mode result. However, at $I_{0L} = 4\times10^{14}$ W/cm^2 there is a sudden increase above the coupled-mode reflectivity. This is the so-called kinetic inflation of SRS. It is due to electron trapping in the Langmuir wave and the resulting decrease of Landau damping.

The time evolution of SRS is then bursty, as illustrated by the plot in Fig. 15 of the instantaneous reflectivity for the inflated case with $I_{0L} = 2\times10^{15}$ W/cm^2, which we label run "SRS1_2." The numerical $R_{\rm av} = 1.03\%$ is well above the coupled-mode level of 6.26×10^{-4}, indicating strong inflation. On a computational note, the phase-space cell advance wall time for this run was 140 ns (compare to 40 ns for the electrostatic run NR1 above). Figure 16 displays the envelope of the longitudinal electric field E_x, which reflects plasma wave activity. Pulses of large-amplitude LWs develop near the laser entrance (the left edge), and then break up into modulations that propagate along "rays" away from the laser entrance with group velocities near v_{Te}. The process repeats once a large enough quiescent plasma develops on the left side. The bursts in $R(t)$ near 3, 6, and 10 ps correspond to large LW pulses on the left edge. The dynamics of these pulses has recently been explained in terms of "etching" at the pulse's left edge, or Landau damping by resonant electrons before they become trapped [45, 46].

For the two strongest pump strengths plotted, $R_{\rm av}$ is actually below the coupled-mode result ("kinetic deflation"). This indicates saturation mechanisms besides pump depletion are important. Both the nonlinear downshift of the Langmuir-wave frequency and the trapped-particle modulational instability [14] are shown to occur to some extent in these runs, although their relative importance has not been quantified.

For trapping nonlinearity to occur, resonant electrons (those moving near the LW phase velocity $v_{p2} = \omega_2/k_2$) must complete enough of a bounce orbit before a detrapping process disrupts their motion. In the SRS1 run series, the only detrapping mechanism that sets a threshold is loss out of the ends of the finite geometry (once large-amplitude waves develop, trapping can be disrupted by various saturation mechanisms and the resulting decrease in wave amplitude). We can estimate a trapping threshold by calculating the "bounce number" N_B, or how many bounce periods a resonant electron undergoes as it transits the domain:

$$N_B(x) \equiv \frac{1}{2\pi}\int_{x_0}^{x} dx'\, k_B(x'), \qquad k_B(x) \equiv \frac{\omega_p}{v_{p2}}[n_2(x)/n_e]^{1/2}. \tag{53}$$

$n_2(x)$ is the local LW amplitude. Inflation will occur if $N_B \gtrsim 1$, such that the electron distribution is sufficiently distorted within the gain region for Landau damping reduction to be effective. The details of finding N_B, using the Langmuir wave driven by the pump and scattered waves as found in the convective coupled-mode theory presented above, are found

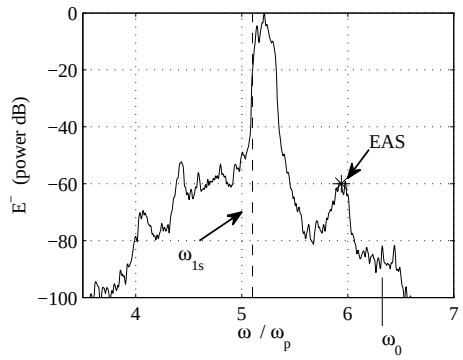

Figure 17. Time-integrated spectrum of reflected light E^- at the left edge for run SRS1_2. The dashed vertical line is the scattered seed $\omega_{1s} = 5.10\omega_p$. Star labeled "EAS" indicates electron acoustic scatter. "Power dB" is $20\log_{10}|E^-(\omega)|$. The pump frequency is $\omega_0 = 6.32\omega_p$.

in Ref. [18]. We just give the result:

$$N_B = N_{Bs}\frac{e^{G/4}-1}{G/4}, \tag{54}$$

$$N_{Bs} = \frac{\omega_p L}{2\pi v_{p2}}(n_{2s}/n_e)^{1/2}, \tag{55}$$

$$n_{2s}/n_e = \frac{(k_2\lambda_D)^2}{2|1+\chi|}\frac{v_{os,0}v_{os,1}}{v_{Te}^2}. \tag{56}$$

N_{Bs} is the bounce number if there were no seed amplification ($G \to 0$).

We briefly discuss the spectral features of the run SRS1_2, and refer the reader to Ref. [18] for details and justification. The time-integrated reflected light spectrum at the left edge is shown in Fig. 17. Since $\omega_0 = 6.32\omega_p$, the SRS light is slightly more than ω_p below ω_0, the difference due to the increase in ω_2 above ω_p due to finite temperature. The peak power is upshifted from the seed value ω_{1s} (the linear most unstable mode) due to the trapping-induced downshift in the LW frequency ω_2. This upshift develops in time, as the LW amplitude grows.

In addition, there is a weak signal labeled "EAS" at a frequency between SRS and ω_0. This is similar in frequency to scattered light observed in the single-speckle Trident experiments [41], although the intensity observed there was only 3000x smaller than SRS (ours is $\sim 10^6$ times smaller). In this paper and elsewhere, the scattered light was attributed to stimulated scattering off an electron acoustic wave (EAW) which becomes undamped once electron trapping occurs. This mode exists as an undamped root of $1+\mathrm{Re}\chi(k,\omega)=0$ with $\omega \approx 1.3kv_{Te}$ (see Refs. [47, 48, 49]). All such roots of the complex Landau dispersion relation $1+\chi=0$ are heavily damped.

We provide an alternative mechanism for generating EAS light, which is revealed by the electrostatic spectrum $E_x(k,\omega)$ presented in Fig. 18. The "Stokes curve" on this plot is the set of (k_2,ω_2) points phase-matched for electromagnetic decay of the pump, that is, $\omega_2 =$

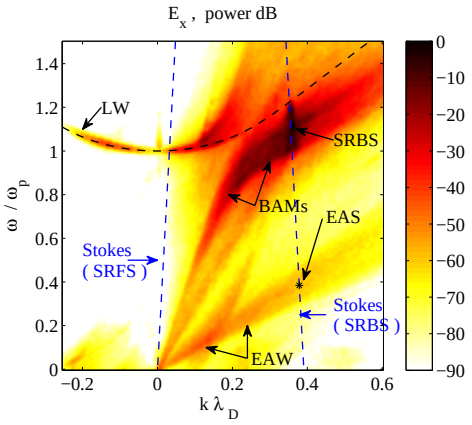

Figure 18. Electrostatic spectrum $E_x(k,\omega)$ over the space-time domain of Fig. 16. SRBS, SRFS label backward and forward SRS, respectively. Black dashed line is the linear Landau LW dispersion curve. Stokes curve (blue dashed line) is defined in the text.

$\omega_0 - \omega_1$ and $k_2 = k_0 - k_1$ with $\omega_1 \in [0, \omega_0]$, $ck_0 = [\omega_0^2 - \omega_p^2]^{1/2}$, and $ck_1 = \pm[\omega_1^2 - \omega_p^2]^{1/2}$ (the +,- root for k_1 apply for forward and backward SRS, respectively). Early in time, SRS occurs at the intersection of the Stokes curve and the linear LW dispersion curve. As electrons are trapped, the LW frequency downshifts along the Stokes curve. The distorted distribution supports a set of beam acoustic modes (BAMs), which are seen as a tail at lower k than the SRS Langmuir wave and lower in ω than the linear dispersion curve. These BAMs can parametrically interact with each other and decay to the acoustic feature $\omega \approx kv_{Te}$, labeled "EAW". We call this process beam-acoustic decay (BAD). The low-k EAWs can produce the higher-k activity along the $\omega \approx kv_{Te}$ line by harmonic generation. The pump laser then scatters off the weak EAW signal on the Stokes curve, in a process akin to Thomson scatter which we refer to as electron acoustic Thomson scatter (EATS). The linear modes of the numerically-obtained distribution (see Fig. 10 of Ref. [18]) include a set of BAMs (some weakly damped or even linearly unstable), as well as a heavily-damped EAW, that agree nicely with the observed $E_x(k,\omega)$ spectrum. The lack of any increase in EAW activity at the Stokes point supports our claim that the observed EAS light is from a Thomson-like process, and not the resonant excitation of an EAW.

The discovery of the BAD-EATS process in ELVIS simulation data, namely weak spectral signals and linear-mode analysis of numerical distributions, constitutes a striking demonstration of the low-noise capability of Eulerian kinetic codes.

4.2. Inclusion of a Krook operator

Thus far the only detrapping process considered is end loss due to finite longitudinal geometry. Finite transverse speckle size (discussed below) also detraps resonant electrons, and is generally much more rapid than end loss. Coulomb collisions also kick electrons out of their bounce orbits and thereby detrap. For a generic detrapping process that removes an electron from resonance in a time t_{de}, we define the bounce number $N_B \equiv t_{de}/\tau_B \propto [\delta n]^{1/2}$ as the number of bounce orbits (period τ_B) completed in t_{de}. We expect trapping nonlinear-

ities to be important only if $N_B \gtrsim 1$. Preliminary work suggests that collisional detrapping is generally much slower than side loss in ICF conditions, unless the plasma is high-Z, or cold and *low* density.

We briefly discuss the speckle pattern of the lasers used on ICF experiments such as NIF. These beams are generally conditioned, or smoothed, with continuous phase plates (CPPs) [50]; random phase plates (RPPs) were common in the past [51]. A phase plate is a lens with a rippled surface (smooth for CPPs, sharp steps for RPPs). Without a phase plate, an ideal optical system would give a diffraction-limited focal spot. But ICF laser systems generate spots far from the diffraction limit, with a generally irregular and difficult to predict pattern of very high-intensity speckles. With the use of a phase plate, one obtains an intensity profile with an envelope much larger than the diffraction limit (set by the lens ripples), and with speckle intensities lower than the unconditioned beam and of well-characterized statistics (the intense speckles are the diffraction-limited spot of the full lens aperture). The ripples on NIF are such that the resulting beam envelope is approximately square. This approach has proven to be more effective than defocusing the original, unsmoothed beam. The intense speckles from a square-aperture phase plate, in use on NIF, are approximately of length $L_{||} \approx 5F^2\lambda_0$ and roughly uniform transverse diameter $L_\perp \approx F\lambda_0$ where $F = L_{\rm foc}/D$ is the F-number of the optics ($L_{\rm foc}$ is the lens focal length and D the lens diameter) [52].

For NIF indirect-drive targets, a grand total of 192 beams are arranged symmetrically about the hohlraum's axis into four cones, making angles of 23, 30, 44, and 50 degrees with respect to the axis. Four $F = 22$ square beams are grouped together in a quad and focused with the same lens (they strike it at different locations), with two beams linearly polarized in each transverse direction (polarization smoothing). In vacuum, all beams overlap in a region between the laser entrance hole and hohlraum wall. Away from this overlap region, the beams diverge. The resulting speckle pattern thus varies in space, based upon how many square beams overlap (either one, two, or four). When four overlap, the speckles "see" the full quad on the lens, the effective beam diameter is about $L_{\rm foc}/8$, and the speckles are cylindrically symmetric with $F \approx 8$. However, for regions covered by two beams or one beam, the speckles are nearly $F = 8$ by $F = 22$ (asymmetric) or $F = 22$ by $F = 22$, respectively. This vacuum propagation picture is further complicated by the presence of plasma, e.g. refraction of light away from high-density regions. Modeling of the 3D laser propagation (and backscatter) in NIF targets, with the paraxial envelope codes PF3D [53, 54] (time-dependent) and SLIP [55, 56] (steady-state), validates this qualitative picture.

In a speckled laser beam, SRS-driven Langmuir waves are of finite size, approximately that of the intense laser speckles. Resonant electrons enter a speckle from the surrounding thermal bath, interact with the wave for a finite transit time, and then leave. Landau damping thus occurs as transit-time damping: free electrons far from the speckle enter the region of Langmuir wave activity, exchange energy by interacting with it, and exit as free electrons. Resonant electrons, moving along ($||$) and across ($\perp$) a speckle with speeds $\approx (v_{p2}, v_{Te})$, have transit times of $\tau_{||} \approx L_{||}/v_{p2}$ and $\tau_\perp \approx L_\perp/v_{Te}$. For a cylindrical, square-lens speckle, $\tau_{||}/\tau_\perp \approx 5Fv_{Te}/v_{p2}$ which is typically $\gg 1$. Thus, transverse side loss is usually much faster than end loss, and is the relevant detrapping time.

Calculations of transit-time damping, using nonlinear electron orbits in a prescribed Langmuir-wave potential that mimics speckle geometry, have been performed by H. Rose [57]. These show the transit-time damping rate decreases slowly with N_B, reaching about

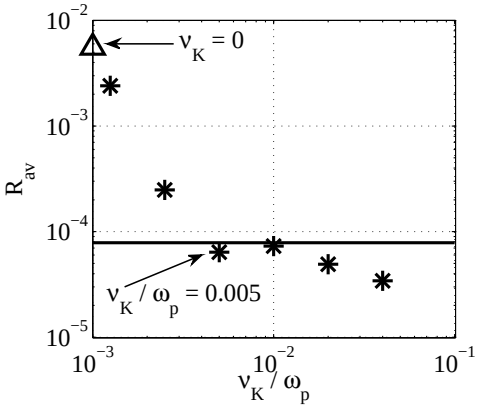

Figure 19. Time-averaged reflectivity $R_{\rm av}$ for run series SRSk (shown as stars), which matches the $I_0 = 10^{15}$ W/cm^2 case from the series SRS1 ($R_{\rm av} = 0.556\%$, shown as the triangle) except that $\nu_K \neq 0$. The solid line $R = 7.86 \times 10^{-5}$ is the steady-state coupled-mode result using linear Landau damping and $\nu_K = 0$.

half its linear value for $N_B = 1$. This quantifies how trapping reduces Landau damping in speckle geometry. Similar work on the nonlinear frequency downshift shows it also turns on slowly with N_B [58]. The damping rate in a finite-geometry speckle becomes more complicated once Langmuir-wave filamentation occurs, and is still under investigation [16].

Speckle side loss can be approximately modeled in a 1D Vlasov code by including a Krook operator, as in ELVIS. We stress that this operator is *not* being used to model collisions, but the transverse loss of electrons from the speckle and their replacement from a thermal (Maxwellian) population. Our Krook operator, which conserves number but neither momentum nor energy, is appropriate for this purpose. The Krook damping rate ν_K is the e-folding time for some perturbation in f_e, so we simply take $t_{de} = 1/\nu_K$ and $N_B = 1/\nu_K \tau_B = (\omega_p/2\pi\nu_K)(\delta n/n_e)^{1/2}$. We have found the time for half the particles of a thermal population to leave a cylinder of diameter $L_\perp$ is $t_{50} v_{Te}/L_\perp \approx (0.68, 0.33)$ in 2D and 3D geometry, respectively. Assuming an exponential decrease of confined particles, these correspond to Krook e-folding rates of $\nu_K = \ln 2/t_{50} = (1.02, 2.10) v_{Te}/L_\perp$.

We examine the role of a Krook operator with the run series SRSk. These runs are like the $I_0 = 10^{15}$ W/cm^2 Krook-free case from the series SRS1 discussed above, except that a nonzero value of ν_K in the central region is used. To give a sense of physically reasonable values for ν_K, we find that for $L_\perp = F\lambda_0$ and the 3D ν_K formula found above, $\nu_K/\omega_p = 2.10\lambda_D/F\lambda_0$. For our Trident-like run conditions and $F = 8$, this gives $\nu_K/\omega_p = 8.26 \times 10^{-3}$. Figure 19 presents $R_{\rm av}$ as a function of ν_K, and shows a gradual decrease of the reflectivity to the coupled-mode value and then below. The coupled-mode result was found with the Krook-free susceptibility χ, and so neglects the increase of damping with ν_K.

We take the case $\nu_K/\omega_p = 0.005$ as a marginal one just below threshold for any inflation. This run's reflectivity becomes relatively steady in time, with the Langmuir wave amplitude fairly uniform in space. We plot the approximate bounce number N_B vs. x, using the spatially local δn for τ_B for this run in Fig. 20. The slight increase, and greater fluctu-

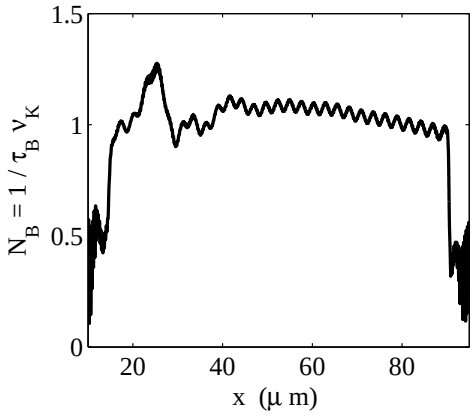

Figure 20. $N_B = 1/\nu_K\tau_B$ for detrapping due to Krook relaxation, for run with $\nu_K/\omega_p = 0.005$ from series SRSk at time 8.8 ps (after steady state has been reached). This case is just below threshold for any SRS inflation. N_B is calculated using the local LW amplitude δn (see text for details).

ations, in N_B toward the laser entrance (left edge) reflect the weak SRS amplification and temporal non-stationarity.

4.3. Inclusion of seed bandwidth

So far, we have always seeded SRS with a monochromatic left-moving seed light wave, with a wavelength chosen to be the temporal most unstable mode. This is similar to the backward Raman amplifier and other "optical mixing" arrangements. However it is unrealistic for ICF, where SRS grows from fluctuations (electrostatic or electromagnetic) in the plasma, or from light or Langmuir waves developing from SRS or other processes outside the spatial region of interest. In this section we show that SRS inflation and the scattered-light spectrum are essentially unchanged when bandwidth is included in the seed light wave. This gives confidence that our prior results are not an artifact of coherent seeding.

Let $f(t) = f_0\cos[\omega_M t + \phi(t)]$ denote the generated signal with bandwidth, which we use for $E^-(t)$ at the right edge. We present an algorithm to find the phase $\phi_n = \phi(t_n)$ on the discrete time grid t_n, such that $|f(\omega)|^2$ is roughly Gaussian with mean ω_M:

$$|f(\omega)|^2 \propto \exp[-(\omega-\omega_M)^2/2\Delta\omega^2]. \tag{57}$$

Our method can be thought of as a discrete analog of a Langevin equation. The ϕ_n satisfy the following recurrence relation:

$$\phi_{n+1} - \phi_n - e^{-1/N}(\phi_n - \phi_{n-1}) = \Delta\omega\Delta t[2N]^{1/2}(1-e^{-1/N})r_n. \tag{58}$$

r_n is a uniform normal deviate of mean zero and variance one, chosen from the probability distribution $P(r) = [2\pi]^{-1/2}\exp[-r^2/2]$. $\Delta\omega$ is the desired spectral bandwidth, and the "phase decay time" $N\Delta t$ ($N \gg 1$ but need not be integer) controls how quickly the instantaneous frequency shift $\alpha \equiv d\phi/dt$ decorrelates. $\Delta\omega$ and N are independent parameters.

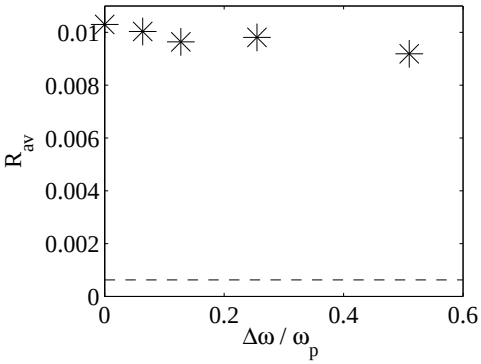

Figure 21. Time-averaged reflectivity $R_{\rm av}$ for run series `Band` vs. scattered-light seed bandwidth $\Delta\omega$. $\Delta\omega = 0$ result is for run `SRS1_2`. Dashed line is linear coupled-mode result $R = 6.26 \times 10^{-4}$ for a monochromatic seed $\Delta\omega = 0$.

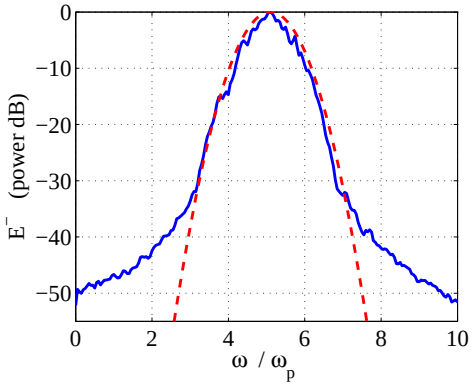

Figure 22. Time-integrated scattered-light seed spectrum for $\Delta\omega = 0.509\omega_p$ run from the series `Band`. The red dashed curve is Eq. (57) for $\omega_M = \omega_{1s} = 5.10\omega_p$.

Different signals can, for infinite time, have similar power spectra, but different rates at which (an appropriately smoothed) α changes. In the context of SRS, we want α to change faster than the SRS growth time, or else SRS will effectively see a relatively monochromatic seed. We implement this method via a fictitious intermediate ϕ':

$$\phi'_{n+1/2} = e^{-1/N}\phi'_{n-1/2} + \Delta t\left(1 - e^{-1/N}\right) r_n; \qquad \phi_{n+1} = \phi_n + \phi'_{n+1/2}. \tag{59}$$

The series of ELVIS runs `Band` illustrates the effect of seed bandwidth. The runs are identical to the run `SRS1_2` except for the inclusion of seed bandwidth (the overall seed intensity is the same, $I_{1R} = 10^{-5} I_{0L}$). For all runs $N\Delta t = 22\omega_p^{-1}$, which is shorter than the undamped growth time $1/\gamma_0 = 43.9\omega_p^{-1}$ from Eq. (49). γ_0 should be an upper bound on the timescale of SRS dynamics, so the seed frequency decorrelates faster than SRS evolves. The time-averaged reflectivity $R_{\rm av}$ for different $\Delta\omega$ is plotted in Fig. 21, and shows only a slight decrease with increasing bandwidth. Figure 22 depicts the time-averaged seed spectrum for the highest-bandwidth case $\Delta\omega = 0.509\omega_p$. It nicely matches the theoretically expected

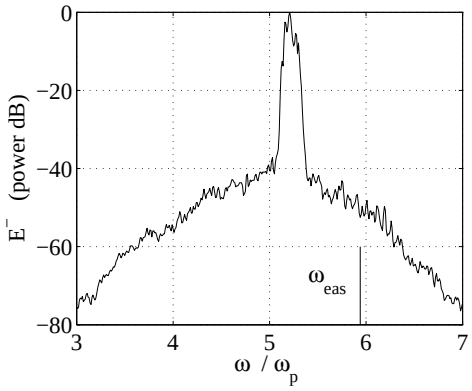

Figure 23. Time-integrated reflected-light spectrum for $\Delta\omega = 0.509\omega_p$ run from the series `Band`. $\omega_{\rm eas}$ is the observed electron acoustic scatter in the run `SRS1_2` from Fig. 17.

Gaussian (the red dashed curve) near ω_M, but has higher tails around the -40 dB level. The reflected light spectrum is displayed in Fig. 23, and shows SRS amplification over a much narrower frequency band than the noise (gain narrowing). Also, there is no distinct electron acoustic scatter (EAS) peak above the seed level, although the $E_x(k,\omega)$ spectrum is similar to the $\Delta\omega = 0$ case shown in Fig. 18 (including the presence of EAWs). This indicates EAS in these runs is not a parametric process that resonantly drives EAWs: if it were, then adding more scattered-light seed by increasing $\Delta\omega$ would increase the EAS level.

5. Conclusion

In this chapter, we presented the 1D Vlasov-Maxwell solver ELVIS. The accuracy of its numerical methods was analyzed, in particular showing the low dissipation and dispersion (and global number conservation) of advection by cubic spline interpolation. The transverse light-wave algorithm was seen to have low dispersion error and no dissipation for $\omega_p\Delta t < 2$.

As an electrostatic application of ELVIS, the evolution of free Langmuir waves, initiated as density perturbations, was presented. For non-relativistic problems, the number and energy conservation and agreement with the linear analytic damping rate were both excellent. Nonlinear damping reduction due to electron trapping was also evidenced. The numerical difficulties due to velocity-space filamentation were seen via the recurrence of the initial perturbation once the recurrence time $t_{\rm rec} = \lambda/\Delta v$ was reached. The Landau damping for relativistic dynamics was shown with ELVIS to be much less than its non-relativistic value, for the high temperature considered (17 keV). Although this is qualitatively like recent analytic results [35], the lack of better agreement may be due to the reduction from 3D to 1D momentum used in ELVIS.

We also discussed several applications to stimulated Raman scattering (SRS). For no Krook operator (outside of boundary regions), the kinetic inflation of SRS above coupled-mode levels occurs. This is due to the trapping-induced reduction of damping. A simple threshold, based upon the number of bounce orbits N_B completed by resonant electrons as they transit the finite gain region, was also given. The modified electron distribution leads to

electrostatic beam acoustic modes, which excite electron acoustic waves (EAWs) by beating with each other. The laser then scatters off these in a Thomson-like way, which is qualitatively similar to (but much lower in amplitude than) the electron acoustic scatter (EAS) observed in Trident experiments [41]. This explanation is distinct from the stimulated EAS picture, where a laser parametrically scatters off (and therefore resonantly excites) an undamped EAW.

These SRS results were then expanded in two ways. Fist, a nonzero Krook rate was included, which provides an inflation threshold. Inflation begins when electrons complete roughly one bounce orbit before being detrapped by Krook relaxation. We discussed how a Krook operator can mimic in 1D the transverse loss of electrons from a laser speckle, and estimated the sideloss escape rate for the phase-plate-conditioned laser beams being used on NIF. The other extension involved using a broadband seed scattered light wave (with Gaussian noise), instead of a monochromatic one. Since ELVIS is very low-noise, some seed level must be included from which SRS can grow. For the inflated case considered, even a large bandwidth ($\Delta\omega = \omega_{1s}/10$) decreased the reflectivity only slightly. This shows that the prior results were not an artifact of a highly coherent seed.

Despite the importance of multi-D effects in SRS, there are still important questions which can be addressed in 1D. The construction and validation of envelope models that can accurately replicate nonlinear kinetic simulations, especially in the onset of inflation, SRS saturation, and resulting scattered light spectra and energetic electron distributions, is a work in progress. Recently, an adiabatic theory of driven Langmuir waves [59] has been applied successfully to the frequency shift [25] and Landau damping reduction [26] in ELVIS simulations of SRS. The results differed from the standard formulas à la Morales [11], and were valid above the so-called "loss of resonance" limit $k_2\lambda_D > 0.53$. A wavenumber, as well as frequency, shift were also observed in these runs.

In addition, little attention has been paid to how trapping affects SRS in an inhomogeneous plasma. Kinetic inflation has been found in ELVIS runs in a density gradient [24, 40], with a somewhat larger reflectivity when the laser propagates toward higher rather than lower density, but a satisfactory understanding is lacking. The competition in SRS of trapping and the Langmuir decay instability (LDI), or decay of a Langmuir wave into an ion acoustic wave and backward-moving Langmuir wave, is also unexplored. This requires mobile ions, which were excluded from the runs presented here. A kinetic (but linear) treatment of LDI was given in Ref. [60]

Use of a range of computational tools, from fluid to Vlasov to particle-in-cell, with varying dimensionality and physics models, will continue to yield new insight into Raman scattering and other processes of basic plasma physics.

6. Acknowledgments

It is with pleasure that we thank M. M. Shoucri, D. Bénisti, J. A. F. Hittinger, H. A. Rose, C. H. Still, and A. K. Ram for assistance, discussions, and support. Work at LLNL partially supported by the U.S. Department of Energy. Figures 14 through 18 reprinted with permission from Ref. [18], Copyright 2007, American Institute of Physics.

References

[1] W. L. Kruer, *The Physics of Laser Plasma Interactions*, Westview Press, Boulder, CO, 2003.

[2] T. Tajima and J. M. Dawson, *Phys. Rev. Lett.* **43**, 267 (1979).

[3] V. M. Malkin, G. Shvets, and N. J. Fisch, *Phys. Rev. Lett.* **82**, 4448 (1999).

[4] S. Atzeni and J. Meyer-ter-Vehn, *The Physics of Inertial Fusion: Beam Plasma Interaction, Hydrodynamics, Hot Dense Matter*, Oxford University Press, Oxford, UK, 2004.

[5] J. Lindl et al., *Phys. Plasmas* **11**, 339 (2004).

[6] J. A. Paisner, E. M. Campbell, and W. J. Hogan, *Fusion Technol*. **26**, 755 (1994).

[7] C. Cavailler, *Plasma Phys. Controlled Fusion* **47**, B389 (2005).

[8] N. B. Mezzan et al., *Phys. Plasmas* **17**, 056304 (2010).

[9] L. D. Landau, *J. Phys. U.S.S.R.* **10** (1946).

[10] T. O'Neil, *Phys. Fluids* **8**, 2255 (1965).

[11] G. J. Morales and T. M. O'Neil, *Phys. Rev. Lett.* **28**, 417 (1972).

[12] R. L. Dewar, *Phys. Fluids* **15**, 712 (1972).

[13] L. Yin et al., *Phys. Plasmas* **16**, 133101 (2009).

[14] S. Brunner and E. J. Valeo, *Phys. Rev. Lett.* **93**, 145003 (2004).

[15] H. A. Rose, *Phys. Plasmas* **12**, 012318 (2005).

[16] H. A. Rose and L. Yin, *Phys. Plasmas* **15**, 042311 (2008).

[17] H. X. Vu, D. F. DuBois, and B. Bezzerides, *Phys. Rev. Lett.* **86**, 4306 (2001).

[18] D. J. Strozzi, E. A. Williams, A. B. Langdon, and A. Bers, *Phys. Plasmas* **14**, 013104 (2007).

[19] S. Brunner et al., Documentation to the SAPRISTI code for kinetic simulations of laser plasma interactions, Technical report, Lawrence Livermore National Laboratory, 2008, Report LLNL-SM-409451.

[20] P. Bertrand et al., *Phys. Fluids B* **2**, 1028 (1990).

[21] A. Ghizzo et al., *J. Comput. Phys.* **90**, 431 (1990).

[22] D. J. Strozzi, *Vlasov Simulations of Kinetic Enhancement of Raman Backscatter in Laser Fusion Plasmas*, PhD thesis, Physics Department, Massachusetts Institute of Technology, 2005.

[23] D. J. Strozzi, M. M. Shoucri, and A. Bers, *Comput. Phys. Comm.* **164**, 156 (2004).

[24] D. J. Strozzi, M. M. Shoucri, A. Bers, E. A. Williams, and A. B. Langdon, *J. Plasma Phys.* **72**, 1299 (2006).

[25] D. Bénisti, D. J. Strozzi, and L. Gremillet, *Phys. Plasmas* **15**, 030701 (2008).

[26] D. Bénisti, D. J. Strozzi, L. Gremillet, and O. Morice, *Phys. Rev. Lett.* **103**, 155002 (2009).

[27] P. L. Bhatnagar, E. P. Gross, and M. Krook, *Phys. Rev.* **94**, 511 (1954).

[28] D. Gabor, *Proc. IRE* **33**, 792 (1945).

[29] N. N. Yanencko, *The Method of Fractional Steps*, Springer-Verlag, New York, 1970.

[30] G. Strang, *SIAM J. Numer. Anal.* **5**, 506 (1968).

[31] C. Z. Cheng and G. Knorr, *J. Comput. Phys.* **22**, 330 (1976).

[32] M. M. Shoucri, *Numerical Solution of Hyperbolic Differential Equations*, Nova Science Publishers, Inc, New York, 2008.

[33] S. Brunner, T. M. Tran, and M. Brunetti, Comparing interpolation methods in the context of solving advection-type equations using the semi-Lagrangian method, internal report, Centre de Recherches en Physique des Plasmas (EPFL, Switzerland), 2005.

[34] C. K. Birdsall and A. B. Langdon, *Plasma Physics via Computer Simulation*, Taylor & Francis Group, New York, NY, 2005.

[35] A. Bers, I. P. Shkarofsky, and M. Shoucri, *Phys. Plasmas* **16**, 022104 (2009).

[36] U. Heinz, *Physics Letters A* **109**, 385 (1985).

[37] G. Hammett, presented at the 18th International Conference on the Numerical Simulation of Plasma, Falmouth, Massachusetts, USA, 2003.

[38] T. Dannert and F. Jenko, *Comput. Phys. Commun.* **163**, 67 (2004).

[39] L. Yin, B. J. Albright, K. J. Bowers, W. Daughton, and H. A. Rose, *Phys. Rev. Lett.* **99**, 265004 (2007).

[40] D. J. Strozzi, E. A. Williams, and A. B. Langdon, *Bull. Am. Phys. Soc.* **51** (2006), Poster UP1.107, APS-DPP 2006, Philadelphia, USA.

[41] D. S. Montgomery et al., *Phys. Rev. Lett.* **87**, 155001 (2001).

[42] D. S. Montgomery et al., *Phys. Plasmas* **9**, 2320 (2002).

[43] J. F. Drake et al., *Phys. Fluids* **17**, 778 (1974).

[44] C. L. Tang, *J. Appl. Phys.* **37**, 2945 (1966).

[45] J. E. Fahlen, B. J. Winjum, T. Grismayer, and W. B. Mori, *Phys. Rev. Lett.* **102**, 245002 (2009).

[46] B. J. Winjum, J. E. Fahlen, F. S. Tsung, and W. B. Mori, *Phys. Rev. E* **81**, 045401(R) (2010).

[47] J. P. Holloway and J. J. Dorning, *Phys. Rev. A* **44**, 3856 (1991).

[48] H. A. Rose and D. A. Russell, *Phys. Plasmas* **8**, 4784 (2001).

[49] F. Valentini, T. M. O'Neil, and D. H. E. Dubin, *Phys. Plasmas* **13**, 052303 (2006).

[50] S. N. Dixit, M. D. Feit, M. D. Perry, and H. T. Powell, *Opt. Lett.* **21**, 1715 (1996).

[51] Y. Kato et al., *Phys. Rev. Lett.* **53**, 1057 (1984).

[52] J. Garnier and L. Videau, *Phys. Plasmas* **8**, 4914 (2001).

[53] R. L. Berger, C. H. Still, E. A. Williams, and A. B. Langdon, *Phys. Plasmas* **5**, 4337 (1998).

[54] D. E. Hinkel et al., *Phys. Plasmas* **15**, 056314 (2008).

[55] P. Michel et al., *Phys. Rev. Lett.* **102**, 025004 (2009).

[56] D. H. Froula et al., *Phys. Rev. Lett.* **100**, 015002 (2008).

[57] H. A. Rose, *Bull. Am. Phys. Soc.* **51** (2006), Talk CO3.10, APS-DPP 2006, Philadelphia, USA.

[58] H. A. Rose, private communication.

[59] D. Bénisti and L. Gremillet, *Phys. Plasmas* **14**, 042304 (2007).

[60] J. P. Palastro, E. A. Williams, D. E. Hinkel, L. Divol and D. J. Strozzi, *Phys. Plasmas* **16**, 092304 (2009).